Chemical Engineering Journal 538 (2026) 176668

Contents lists available at ScienceDirect

Chemical Engineering Journal

journal homepage: www.elsevier.com/locate/cej

Conversion of agricultural waste into green–white graphene hybrids for high-performance textiles

Moumita Kotal [a,1,*], Guilherme da Silva Lopes Fabris [b,1], Surbhi Slathia [c], Akbar Shanu [d], Rakesh Das [a], Bruno Ipaves [b], Marcelo Lopes Pereira Júnior [e,f], Bidush Das [g], Jayanta Bhattacharya [g], Sajith Vandana [d], Douglas Soares Galvão [b,*], Chandra Sekhar Tiwary [a,c,*]

[a] Department of Metallurgical and Materials Engineering, Indian Institute of Technology Kharagpur, 721302, West Bengal, India
[b] Applied Physics Department and Center for Computational Engineering & Sciences, State University of Campinas, Campinas, SP, 13083-970, Brazil
[c] School of Nano Science and Technology, Indian Institute of Technology Kharagpur, 721302, West Bengal, India
[d] Department of Materials Science and Engineering, National Institute of Technology Calicut, Kerala, 673601, India
[e] University of Brasília, College of Technology, Brasilia, DF, 70910-900, Brazil
[f] Materials Science and Nano Engineering Department, Rice University, Houston, TX, 77005, USA
[g] Zelence Industries Pvt Ltd, Science and Technology Entrepreneurs Park, Indian Institute of Technology Kharagpur, 721302, West Bengal, India

ARTICLE INFO

Keywords:
High-performance textiles
Green graphene
Hexagonal boron nitride
Flame retardancy
Hydrophobic
Mechanical durability
Molecular dynamics simulation

ABSTRACT

Transforming agricultural waste into functional nanomaterials offers a sustainable and value-added approach for developing next-generation high-performance textiles. Here, aminated green graphene (AGG), derived from agricultural biochar, is integrated with hydroxylated hexagonal boron nitride (h-BN–OH, "white graphene") to engineer a dual hybrid coating on cotton fabrics (CFs). The synergistic AGG–h-BN–OH architecture forms a robust interfacial network through hydrogen bonding, electrostatic, and π–π interactions, imparting outstanding multifunctionality. The optimized CF/4AGG–h-BN–OH exhibits exceptional mechanical strength (24.5 MPa, ~171% improvement) and toughness (2.91 MJ m^{-3}, 246% improvement), along with hydrophobicity (water contact angle = 129°), superior thermal stability (28 wt% char residue at 700 °C), prolonged heat transfer time (32 s vs. 10 s for pristine CF), significantly improved LOI% (30.2 vs. 19.1 for CF) and reduced char length (2.4 cm vs. full length for pristine CF). The fabric also offers significant antibacterial activity against both Gram-positive and Gram-negative bacteria and promising water-immersion stability. Mach–Zehnder interferometric analyses reflect excellent thermal-shielding efficiency, while molecular dynamics simulations indicate that dual coating of cellulose with AGG and h-BN–OH enhances structural stability at the atomistic scale through synergistic physical shielding and reduced molecular mobility, consistent with delayed structural disruption and a lower propensity for volatile species formation. Collectively, this halogen-free, bio-derived hybrid technique valorises agricultural wastes into advanced graphene-based coatings, pioneering a scalable approach toward the development of high-performance, flame-retardant, and antibacterial cotton fabrics for applications in healthcare, protective clothing, and aerospace textiles.

1. Introduction

The development of sustainable textile products is urgently required owing to the rising environmental pollution, disruption of ecological equilibrium, and growing demand for improved quality of life, especially in crucial sectors like healthcare, sanitation, and filtration. Cotton fabrics (CFs), the most extensively employed natural textiles, are recognized for their breathability, affordability, thermal comfort, and dyeability. However, their safe and long-term use is restricted because of their inherent limitations-large hydrocarbon content rendering them

* Correspondence to: M. Kotal, Department of Metallurgical and Materials Engineering, Indian Institute of Technology Kharagpur, 721302, West Bengal, India; D.S. Galvão, Applied Physics Department and Center for Computational Engineering & Sciences, State University of Campinas, Campinas, SP, 13083-970, Brazil; C.S. Tiwary, Department of Metallurgical and Materials Engineering, Indian Institute of Technology Kharagpur, 721302, West Bengal, India.
E-mail addresses: moumita.kotal@gmail.com, moumita25@kgpian.iitkgp.ac.in (M. Kotal), galvao@ifi.unicamp.br (D.S. Galvão), chandra.tiwary@metal.iitkgp.ac.in (C.S. Tiwary).
[1] M.K. & G. S. L. F are joint first authors

https://doi.org/10.1016/j.cej.2026.176668
Received 10 December 2025; Received in revised form 3 April 2026; Accepted 23 April 2026
Available online 24 April 2026

highly flammable, causing serious fire hazards, while their hydrophilic feature (presence of cellulose) assists contamination and bacterial growth, leading to risks to human health. These drawbacks highlight the pivotal necessity for designing multifunctional CFs featuring flame-retardant, hydrophobic, and antibacterial properties [1–3]. Additionally, the growing demand for mechanically resilient CFs emphasizes the significance of designing robust, high-performance textiles from sustainable feedstocks with the least environmental impact, appropriate for applications in aerospace, medical emergencies, and defense.

To date, the most effective approaches to develop flame-retardant, hydrophobic, and antibacterial CFs are surface modification techniques, like dip-coating, chemical grafting, sol-gel, layer-by-layer assembly and layer-by-layer deposition techniques [4–8]. Epoxy resins and adhesives have also been employed to enhance water resistance and mechanical resilience, but they are inherently flammable and therefore unsuitable for flame-retardant applications [9]. Alternatively, polymers such as branched poly(ethylenimine), poly[1,4-diaminophenylene-tris (dimethylhydroxymethyl)phosphine], and poly(allylamine) have been incorporated via layer-by-layer assembly to achieve flame retardancy [10–12]. Although these approaches significantly improve the flame-retardant and hydrophobic performance of CFs, their long-term durability remains limited, as most coatings rely on weak physical adsorption to the cotton surface.

In response, recent efforts have shifted toward covalently attaching flame-retardant and hydrophobic moieties to CFs, offering improved stability and wash resistance. For example, silicone finishing agents modified with fluorinated phosphate acid esters, hexafluorophosphoric acid, and bis(trifluoromethane)sulfonamide lithium have been explored to produce durable multifunctional CFs [13,14]. However, halogen-based flame retardants have been largely discontinued owing to their tendency to release toxic and persistent by-products such as dioxins during combustion. Recently, Qian et al. developed highly stable, antibacterial CFs through employing molecular engineering approaches where copper ions formed strong coordination bonds with the oxygen-containing polar groups (e.g., hydroxyl) of the cellulose chains [15]. However, the use of Cu in developing antibacterial CFs is limited by cytotoxicity, environmental concerns from ion leaching, poor durability under washing, and adverse effects on fabric aesthetics and safety. Consequently, the development of halogen-free, renewable, and non-toxic alternatives is urgently needed to design multifunctional CFs that combine durability with structurally robust, flame-retardant, hydrophobic, and antibacterial features.

The use of biochar, a carbonaceous solid product of biomass pyrolysis, has been investigated as a promising, eco-friendly, and economically viable approach for achieving sustainable multifunctional CFs. According to the 2018 IPCC report, it has proved to be an effective negative emitter of harmful greenhouse gases [16]. In particular, biochars obtained from agricultural biomass, called ‘green graphene’, have several benefits over direct combustion, such as long-term carbon content, large surface area, fossil energy offsets, and thermal stability [17]. Moreover, the presence of intrinsic elements like P, N and S facilitates flame-retardant mechanisms, while the increased oxygen availability accelerates char formation during combustion, further promoting fire resistance [18]. Moreover, biochar can disperse effectively in water, reducing the need for organic solvents and minimizing environmental impact, and its diverse functional groups facilitate strong binding with other elements, leading to the formation of stable hybrid structures. In parallel, hexagonal boron nitride (h-BN) is an environmentally friendly chemical compound, an isoelectric analog of graphene, called ‘white graphene’, that exhibits several interesting properties, including excellent barrier diffusion, high thermal stability and conductivity, mechanical robustness, and flame-retardant capability [19]. Also, the high surface area, flexibility, and capability to develop thermally stable char after combustion are the added benefits to develop multifunctional CFs.

Herein, an innovative sustainable approach using environmentally friendly, halogen-free functionalized green graphene (GG) and white graphene (h-BN) has been designed to develop micro-nano coated porous CFs using a dipping chemical reaction method for the exploration of flame-retardant, hydrophobic, mechanically strong, thermally stable, and antibacterial CFs. GG (biochar from the agricultural waste), which contains a large number of oxygen atoms, has been functionalized with flame-retardant, eco-friendly diethylenetriamine (DETA) as illustrated in Fig. S1, while h-BN has been hydroxylated in air at high temperatures. Such sustainable functionalization techniques are advantageous for H-bonding interactions with CFs, and the opposing surface charges enhance strong electrostatic interactions between amine-functionalized GG (AGG) and hydroxylated hBN (hBN-OH). Also, π-π stacking interactions between functionalized GG and h-BN are not ruled out. As a result, a homogeneous distribution of h-BN-OH and AGG over CF facilitates the formation of a uniform char layer during combustion, effectively inhibiting heat propagation and enhancing flame-retardant response. Moreover, such a uniform distribution not only facilitates strengthening the CF for offering emerging mechanical resiliency but also acts as a barrier by reducing the interaction of CFs with water. Also, such interactions between AGG and hBN-OH with cellulose chains directly damage bacterial cell membranes and hinder bacterial cell growth, resulting in significant antibacterial activity. Therefore, we anticipate that our facile, viable approach (as illustrated in Scheme 1a) presents a unique and potential way to the design of efficient, multifunctional CFs with remarkable flame-retardancy, promising mechanical resiliency, emerging hydrophobicity, and significant antibacterial activity. Scheme 1b depicts a radar plot outlining the multifunctional performance of pristine and AGG/h-BN–OH-coated cotton fabrics. The engineered coated fabric shows a promising enhancement in all aspects, including mechanical strength, toughness, hydrophobicity, thermal stability, flame retardancy, and antibacterial effectiveness. This innovative strategy explores the sustainable potential of cellulosic materials, expanding their effectiveness toward improving public health, safety, and environmental well-being.

2. Experimental section

2.1. Materials

Hexagonal boron nitride (h-BN) was obtained from Vedayukt India Pvt. Ltd., and diethylenetriamine (DETA, ≥99%) from Sigma-Aldrich. Agricultural waste–derived biochar was used as the precursor for green graphene (GG). White cotton fabric (54″ × 90″, 120 thread count) served as the substrate. Deionized water was supplied by a Milli-Q purification system. *Staphylococcus aureus* (ATCC 25923) and *Escherichia coli* (ATCC 25922) were used for antibacterial testing. All chemicals were reagent grade and used as received.

2.2. Synthesis of green graphene and aminated green graphene (AGG)

Green graphene was prepared from biochar following a previously reported method [20]. The obtained GG was functionalized by refluxing with DETA to yield aminated green graphene (AGG). Detailed synthesis protocols and purification steps are illustrated in the Supporting Information.

2.3. Preparation of hydroxylated h-BN (h-BN–OH)

In order to introduce hydroxyl functional groups on the surface of pristine h-BN, thermal activation was performed, followed by washing repeatedly. The complete synthesis parameters and optimization conditions are provided in the Supporting Information.

2.4. Fabrication of AGG/h-BN–OH Hybrid-Coated CFs and their individual coatings

CFs were soaked in a dilute alkali solution to increase surface

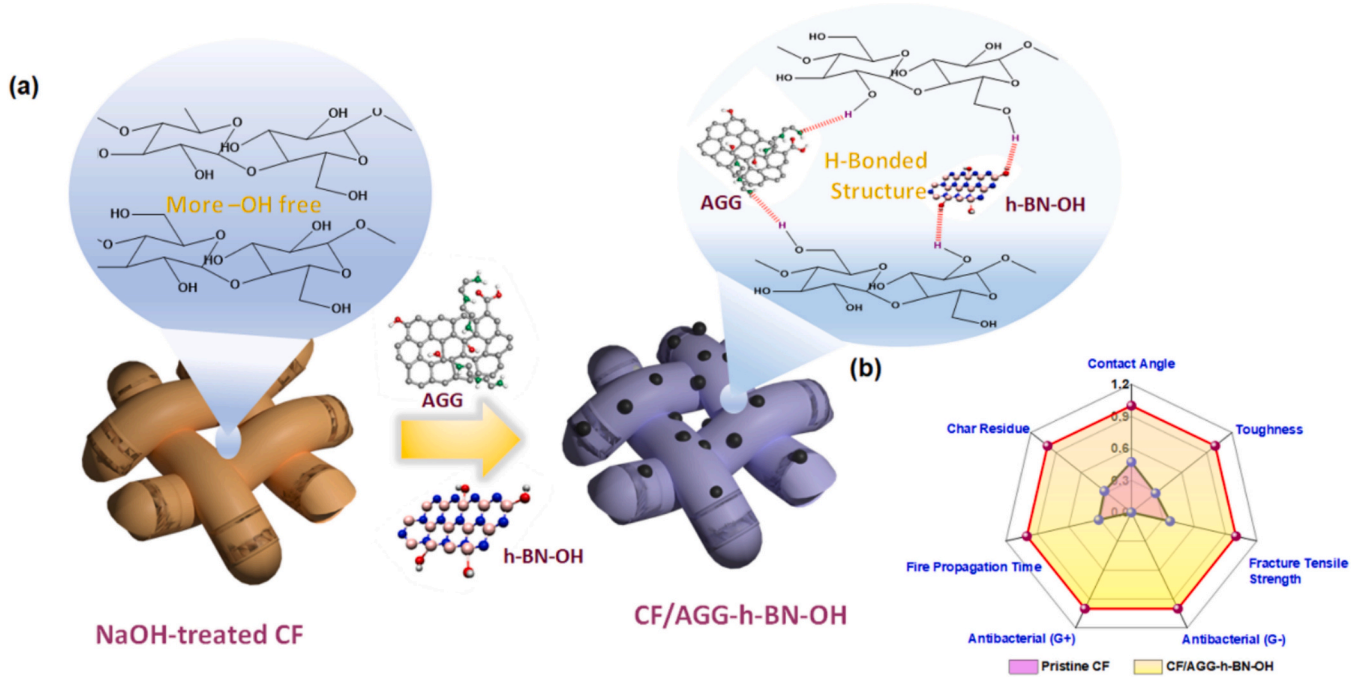

Scheme 1. a) Schematic illustration for the interaction of alkali-treated Cotton fiber with aminated green graphene (AGG) and hydroxylated hexagonal boron nitride (hBN-OH) through H-bonding (red atoms-O, green atoms-N, gray atoms-C, white atoms-H for AGG and pink atoms-B, blue atoms-N, white atoms-H for hBN-OH); b) Radar plot comparing the multifunctional performance of pristine and treated cotton fabrics. To enable comparison of properties (mechanical properties, hydrophobicity, flame retardant responses, and antibacterial activity) with different units, all values were normalized with respect to the treated fabric (treated = 1), highlighting the relative enhancement achieved through treatment.

reactivity. The alkali-treated fabrics were dipped in mixed aqueous suspensions of AGG and h-BN–OH at specified ratios (2, 4, and 6 wt%). Subsequently, the coated fabrics were subjected to heating for strengthening interfacial bonding, followed by drying at a controlled temperature to verify stable adhesion of the hybrid layer. The complete coating procedure, composition optimization, and post-treatment steps are included in the Supporting Information.

2.5. Water-immersion stability tests

The coated fabrics underwent repeated water-washing cycles under controlled conditions to investigate coating stability without employing a binder. Mechanical strength, hydrophobicity and flame retardancy were investigated after 10 and 20 repeated water-immersion and drying cycles.

2.6. Characterization techniques

Structural and chemical functionalities were evaluated using FTIR, XRD, Raman spectroscopy, XPS, SEM, optical microscopy, and particle size/zeta potential measurements. Surface wettability, mechanical properties, and thermal stability were measured using standard instruments. Detailed instrument models, calibration protocols, and test parameters are provided in the Supporting Information.

2.7. Mach–Zehnder Interferometry

Thermal-shielding performance was evaluated using a Mach–Zehnder interferometer. Fringe distortion and wavefront deviation were used to quantify convective and conductive heat-transfer behavior. The complete optical setup, alignment procedure, and data-processing methodology are presented in the Supporting Information.

2.8. Computational methods

Reactive molecular dynamics (ReaxFF) simulations were performed using LAMMPS to understand heat-induced degradation pathways of cellulose in the presence of h-BN–OH and AGG. Model construction, force-field parameters, simulation conditions, and analysis workflows are provided in the Supporting Information.

3. Results & discussion

3.1. Structural, chemical and dispersion characterization

To verify the amine functionalization in GG, FTIR spectra of GG and AGG were recorded, as shown in Fig. S2a. A strong band appeared at around 1570 cm^{-1} corresponding to C═C stretching variation in aromatic rings, suggesting the appearance of a honeycomb-like structure in GG after pyrolysis. The peak at around 1396 cm^{-1} can be assigned to the $–CH_2$ deformation. The strong band at about 1052 cm^{-1} could be attributed to the alcoholic C—O stretching vibration. Furthermore, the bending vibration of Si-O-Si appeared at 466 cm^{-1}. The broad peak corresponding to –OH arises at 3432 cm^{-1}. Interestingly, in the case of AGG, along with –OH and C═C stretching vibrations, the peaks appeared at around 3370 cm^{-1}, 1532 cm^{-1} corresponding to -NH stretching and –NH bending vibrations, respectively, thus confirming the successful functionalization of the amine group in GG [21]. Also, the peak at around 1050 cm^{-1} is found to be relatively broader owing to the presence of both C—N and C—O stretching vibrations, respectively, in AGG, reaffirming our earlier findings. Moreover, the band of asymmetric –NH stretching was also found at 806 cm^{-1}, indicating successful amine functionalization. On the contrary, h-BN was oxidized to introduce –OH groups at the edges of h-BN layers. FTIR spectra of both h-BN and h-BN-OH were compared to investigate the covalent hydroxylation of h-BN layers, as depicted in Fig. S2b. The comparatively broader peak appeared at around 3288 cm^{-1}, corresponding to B-OH stretching vibrations. Apart from B—N stretching at 1306 cm^{-1} (1330 cm^{-1} for h-

BN) and B—N bending around 806 cm^{-1} (765 cm^{-1} for h-BN), which are the characteristic peaks of BN, new peaks appeared at around 1453 cm^{-1}, 1205 cm^{-1}, and 846 cm^{-1} representing B—O stretching, B—O in-plane bending, and B-OH out-of-plane bending vibrations, respectively [22]. The increase in intensity ratio of –OH stretching and B—N stretching in h-BN-OH (0.4716) compared to h-BN (0.0315) further confirms successful hydroxylation in h-BN sheets.

Such a type of functionalization of GG and h-BN was useful to coat them over CF through electrostatic interaction, as evident from the zeta potential of AGG (−10.2 ± 0.5 mV) and h-BN-OH (−36.5 ± 1.3 mV). Notably, zeta potential is found to be more positive after amine functionalization in GG compared to GG itself (−27.3 ± 0.8 mV) owing to the availability of the positively charged amine group through replacing epoxy groups in GG, while zeta potential is observed to decrease after introducing –ve charged hydroxyl group in h-BN layers compared to h-BN itself (−1.5 ± 1 mV). Interestingly, after functionalization, the particle size is found to decrease significantly, with AGG exhibiting an average diameter of 0.66 μm, compared to 1.618 μm for GG-750, as shown in Fig. S3a. The absence of larger macro-sized particles in AGG indicates successful exfoliation and surface modification, which enhances its colloidal stability and promotes uniform dispersion in the coating solution. This improved homogeneity facilitates strong and continuous coating formation on the cotton fibers, as discussed in the subsequent morphological analyses. Noticeably, after hydroxylation of h-BN, particles are found to distribute from 0.08 μm to 0.51 μm and the availability is higher, as presented in Fig. S3b.

To ensure the successful coating of AGG and h-BN-OH over CF, FTIR spectra (Fig. 1a) were recorded for untreated CF and coated CF with varying content of AGG and h-BN-OH [1:1 with varying concentration-7 mg ml^{-1}, 10 mg ml^{-1}, and 15 mg ml^{-1} to provide AGG/hBN-OH content of 2, 4, and 6 wt%]. The spectrum of CF presents peaks at 3329 cm^{-1} related to the –OH groups of cellulose, 1715 cm^{-1} corresponding to –C=O stretching, 1039 cm^{-1} assigned to C—O stretching vibrations, and a band at 870 cm^{-1} originating from the β-linkage of

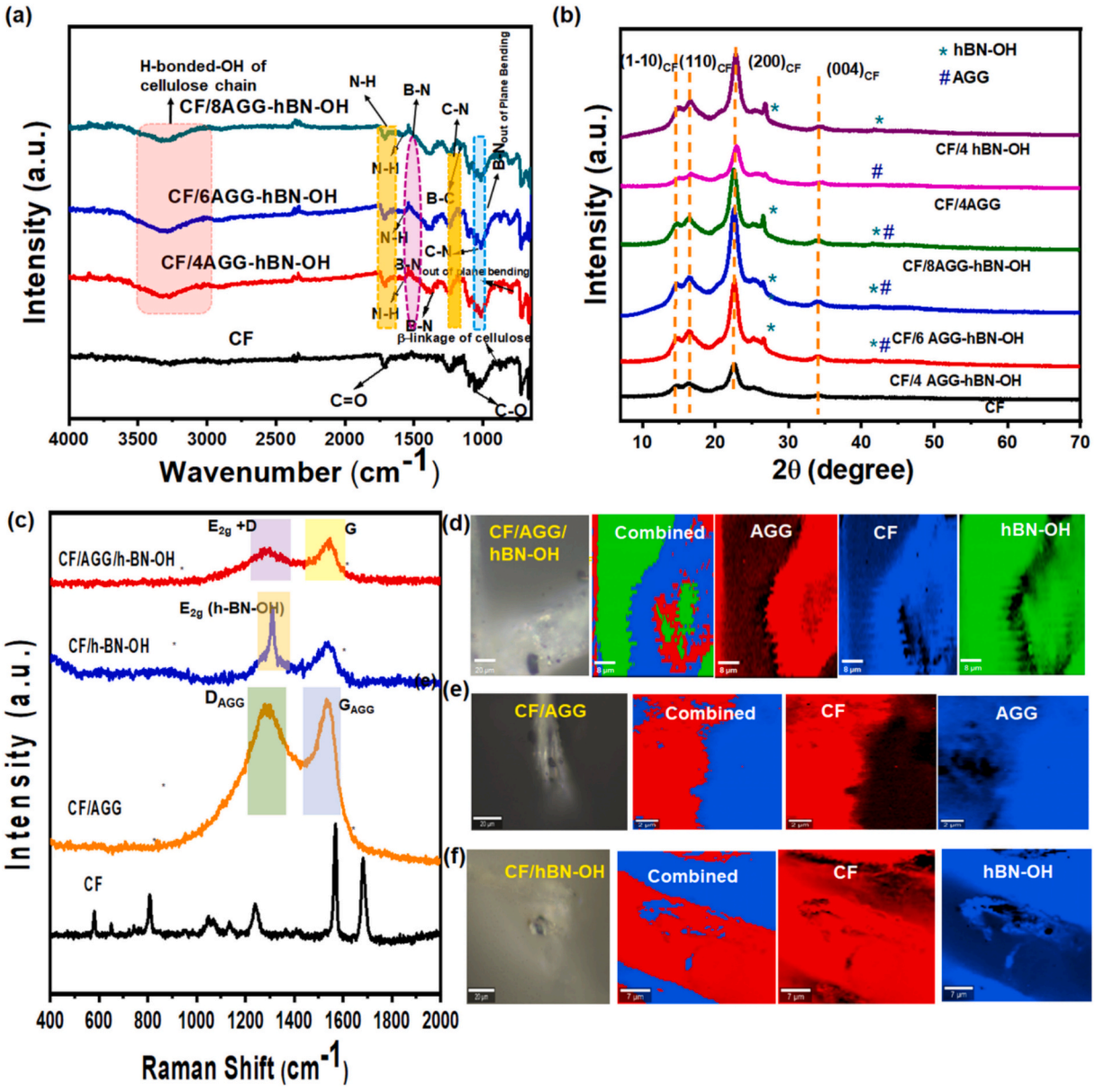

Fig. 1. Structural characterizations of pristine CFs, individual coating of AGG (or hBN-OH) at 4 wt%, and their hybrid coating on CFs at varying wt%- a) FTIR spectra and b) XRD patterns. c) Raman spectra of CF, AGG coated CF, hBN-OH coated CF, and AGG/hBN-OH-coated CF; Raman Mapping of d) AGG/hBN-OH-coated CF to identify the individual dispersion of each component-Red region for AGG, Green region for hBN-OH, and blue region for CF, e) AGG-coated CF-red region for CF and blue region for AGG, and f) hBN-OH-coated CF-red region for CF and blue region for hBN-OH.

cellulose. Interestingly, after the coating of AGG and h-BN-OH, in every case, several new peaks appeared like peaks corresponding to –NH, B—N, C—N stretching and B—N out-of-plane-bending vibrations, confirming the presence of both aminated green graphene (AGG) and h-BN-OH, which infers their successful decoration in CF. Moreover, the intensity of H-bonded –OH of cellulose chain is found to increase in the decorated CF owing to the H-Bonding of -OH of h-BN-OH and $–NH_2$ (or –NH) of AGG individually with cellulose chain of CF, which contributes to strengthening the CF in physico-mechanical respect.

X-ray diffraction patterns were used to analyze the change in crystal structure after hydroxyl and amine functionalization in h-BN and GG, respectively. XRD of GG and amine-functionalized GG, as illustrated in Fig. S2c, shows the presence of a broad diffraction peak of 2θ centered at 23° in GG corresponding to the (002) plane shifted to 21.8° after functionalization (AGG), suggesting increased interlayer distance through incorporating $–NH_2$ in GG layers [23]. Interestingly, the sharp diffraction peak of 2θ at 28.1° corresponding to (111) plane of SiO_2 in GG is found to be absent in AGG, indicating successful removal of SiO_2 during washing, which is highly advantageous to investigate the effect of functionalization in GG on hydrophobicity and flame-retardant behavior of CF, as the presence of SiO_2 can offer erroneous results [20]. Also, there are a few sharp intensity peaks in GG, which are found to be absent in AGG, except a small hump at 43°, revealing the presence of amorphous carbon having honeycomb structures formed by sp^2 hybridization [23]. XRD patterns of h-BN and h-BN-OH, as presented in Fig. S2d, reveal that both exhibit good crystallinity, suggesting that the crystalline structure of h-BN remains even after the hydroxylation process. h-BN shows several diffraction peaks centered at 2θ of 26.48°, 41.4°, 43.8°, 50.1°, and 54.96°, corresponding to (002), (100), (101), (102), and (004) planes, respectively. Noticeably, after hydroxylation, the diffraction peak corresponding to the (002) plane shifted to a comparatively lower angle of 26.3° with lower intensity, suggesting an increased interplanar distance through introducing –OH groups on the edge of h-BN layers [24]. The intensity of other diffraction peaks is also decreased after hydroxylation, reaffirming our earlier findings. These findings further indicate less ordered stacking along the z-direction after hydroxylation, which indirectly demonstrates their effective exfoliation during coating over CF. Such functionalization of GG and h-BN is advantageous for coating over CF through H-bonding to enhance the hydrophobicity, mechanical, and flame-retardant responses, which are discussed later.

In order to investigate the existence of AGG and hBN-OH in the coated CF, XRD patterns of untreated CF and individual AGG or hBN-OH treated CF and synergistically treated CF are displayed in Fig. 1b. Notably, in each case XRD peaks corresponding to CF are present centering at 2θ of 14.5°, 16.48°, 22.7° and 34.3° associated with (1−10), (110), (200) and (004) crystal faces, respectively [25]. Furthermore, XRD patterns of CF are almost similar to CF/ 4AGG, except for the broad peak at 2θ of 43° corresponding to the (100) plane of AGG inferring that AGG could not influence the crystal structure of CF. Also, it is observed that the (200) plane of CF is quite widened as the (002) plane of AGG is almost at a similar position to the (200) plane of CF. Interestingly, for AGG/hBN-OH-coated CF, characteristic peaks of both hBN-OH and AGG are present, confirming their successful decoration over CF. Similar findings have also been noted for hBN-OH-coated CF.

Raman spectra of AGG/h-BN-OH-coated cotton fabrics (CF) along with their individual counterparts like AGG (or h-BN-OH)-coated CF are investigated to reveal their successful coating, as presented in Fig. 1c. Notably, AGG-coated CF showed two characteristic broad peaks at 1290 cm^{-1} (D-band) and 1540 cm^{-1} (G-band), respectively, confirming the presence of AGG over CF. The broad D-band is related to C atoms of defects arising from the H-bonding interaction of aminated biochar (AGG) with oxygen-containing groups in the cellulose, while the wide G-band depicts carbon atoms with sp^2 electronic configuration [26]. Raman mapping (Fig. 1e) further confirms that the presence of two components in the AGG-coated CF-blue region is for AGG, and the red region is for CF. In the case of h-BN-OH–coated CF, a sharp peak observed at 1310 cm^{-1} corresponds to the E_2g vibrational mode of h-BN, arising from B—N bond stretching. Interestingly, a blue shift is observed after exfoliation of h-BN-OH (1332 cm^{-1}) during coating over CF, suggesting that the number of h-BN layers is decreased. Raman mapping also reveals the presence of h-BN-OH flakes over CF, as displayed in the blue region (h-BN-OH) and red region (CF) in Fig. 1f. However, AGG/h-BN-OH-coated CF exhibits comparatively two wider peaks with lower intensity- D band of AGG and E_{2g} vibrational mode of h-BN-OH at 1290 cm^{-1} and G-band at 1545 cm^{-1} of AGG. Owing to the high intensity of the AGG peak, almost at a similar position, the h-BN-OH peak is not found to be prominent in AGG/h-BN-OH-coated CF. Such wider peaks could be attributed to the strong interfacial interaction of AGG and h-BN-OH with CF, as evident from previous findings. Also, red shifting of G-band by 5 cm^{-1} compared to AGG-coated CF, further reaffirms the interaction of AGG and h-BN-OH with CF, which is a critical prerequisite for synergistic improvement in mechanical properties, hydrophobicity, and flame-retardant responses. Additionally, the peaks related to CF in all three cases are present with decreased intensity, indicating successful decoration of AGG/h-BN-OH (or their individual counterpart) over cotton fabric. Raman mapping (Fig. 1d) further reveals the homogeneous distribution of AGG and h-BN-OH over CF-red region for AGG, green region for h-BN-OH, and blue region for CF.

To investigate the chemical interactions of AGG and h-BN-OH with cotton fabrics, as well as their efficient coating, XPS of untreated CFs, individual AGG, and its hybrid with h-BN-OH decorated CFs, have been recorded (Fig. 2a-g). XPS survey spectra indicate an increase in carbon content from 59.4% for pristine CFs to 68.11% for AGG-coated CFs. On the other hand, a decrease in oxygen content from 40.6% to 28.97% was observed, suggesting the presence of more AGG flakes on the fiber surface. Moreover, the content of N (2.95%) incorporation confirms successful coating of AGG on CFs. Notably, owing to the presence of h-BN-OH in AGG/h-BN-OH coated CFs, the higher content of N (33.05%) and B (28.82%) suggests their homogeneous decoration on CFs. The high-resolution C1s spectra for each CFs, for untreated and treated CFs, as presented in Fig. 2b-d, depict three peaks corresponding to C—C (284.5 eV), C—O (hydroxyl, 285.87), and O-C=O (287.69 eV). Interestingly, C-O/C-N content is found to gradually increase from pristine CFs (35.45%) to AGG decorated CFs (42.74%) to AGG/h-BN-OH coated CFs (50.79%), reaffirming the presence of AGG/h-BN-OH (or AGG) flakes in the fibers. Furthermore, the higher concentration of two fitted peaks (C—N or B-N: 398.4 or 397.1 eV, and N-H: 399.3 eV) for high-resolution N1s spectra of AGG/h-BN-OH coated CFs compared to AGG coated CFs, reveals the presence of h-BN-OH together with AGG in the former coated CFs (Fig. 2e, f). The high-resolution C1s, N1s, and B1s spectra for AGG/h-BN-OH hybrid are also presented in Fig. S4a-c to understand their interaction with CFs. Notably, N—H peak is found to shift from AGG/h-BN-OH hybrid (398.80 eV) (Fig. S4b) to 399.22 eV, for the corresponding coated CFs with increased intensity, confirming the presence of H-bonded N after coating on CFs [27]. This is attributed to the formation of H-bonding where –OH of cellulose chains of CFs behaved as H-donor and –NH of AGG acted as H-acceptor or –NH2 of AGG as H-donor and –OH of cellulose chains of CFs as H-acceptor. H-bonding can occur from donation of H from –OH of h-BN-OH to –OH of cellulose chain of CFs, as evident from the shifting of B—O (i.e., B-OH) peak from 190.49 eV for AGG/h-BN-OH hybrid to 191.27 eV, in the corresponding coated CFs with increased intensity (Fig. S4c) [28]. Such a type of multiple H-bonding interaction facilitates strengthening the CFs and makes them durable even after repeated washings. To understand the surface morphology of untreated and treated CFs, optical microscopy and SEM images have been recorded, as illustrated in Fig. 2h-j. Notably, the surface of the fiber of pristine CFs is smooth and planar with a width of 12.875 μm (Fig. 2h), while after AGG/h-BN-OH coating (Fig. 2i), the width is found to increase uniformly (25.579 μm), suggesting a stronger interaction of AGG and h-BN-OH with CFs through intermolecular H-bonding and electrostatic interaction, which supports our earlier

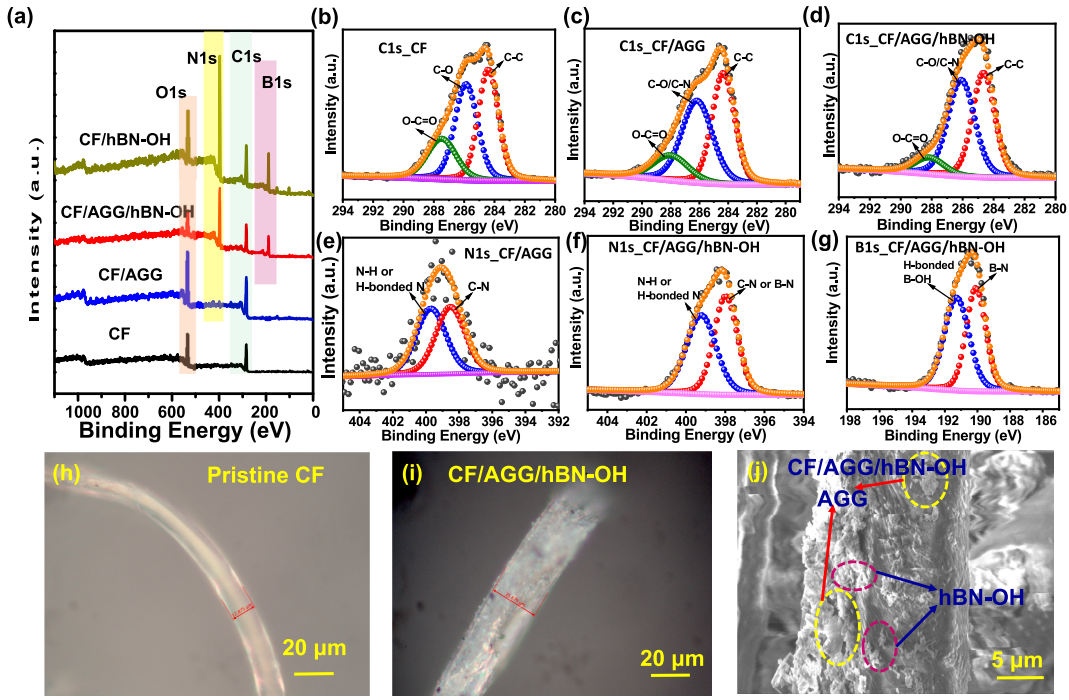

Fig. 2. Structural and morphological analyses of untreated and treated CFs: a) XPS survey spectra of pristine CFs and AGG, h-BN-OH individually and their hybrid coated CFs; high-resolution C1s spectra of b) CF; c) AGG coated CFs and d) AGG/h-BN-OH-coated CFs; high-resolution N1s spectra of e) AGG coated CFs and f) AGG/h-BN-OH-coated CFs and g) high-resolution B1s spectra of AGG/h-BN-OH-coated CFs; Optical microscope images of h) pristine CFs and i) AGG/h-BN-OH-coated (4 wt %) CFs showing almost two times increase in width and j) SEM image of AGG/h-BN-OH-coated (4 wt%) CFs showing uniform decoration of both h-BN-OH and AGG over the fiber.

findings. However, at higher concentration coating of AGG/h-BN-OH, the coated fiber shows aggregation (Fig. S4d). SEM image of the coated fabric shows homogeneous distribution of AGG and h-BN-OH over the fibers (Fig. 2j and Fig. S4e), which is advantageous to develop multifunctional CFs. At higher magnification, it shows significant covering of AGG with h-BN-OH through strong electrostatic and π-π stacking interactions (Fig. S3f), benefiting the development of durable CFs even after repeated washings.

3.2. Surface wettability and hydrophobic behavior

The surface wetting property of AGG/hBN-OH decorated CF, along with their individual coating, was examined by water contact angle (CA) measurements. Fig. 3a shows the water contact angle variation for each coated cotton fabric along with the corresponding photographs of water droplets. It is noticed that pristine CF exhibited a CA of 61°, showing immediate penetration of water droplets into the CF owing to the capillary effect affected by porosity and abundant hydroxyl groups on the fabric. AGG-coated CF with varying wt% (4 and 6 wt%) showed CA of 75° and 90° due to the increased surface roughness through homogeneous distribution of AGG over CF. However, such improvement in CA is not very significant, as GG was modified by DETA, leading to some free amine functional groups surrounded by GG. On the contrary, h-BN-OH coated CF exhibited a CA of 115° owing to the synergy of the nanoscale roughness of h-BN-OH and the inherent hydrophobicity of h-BN. Interestingly, AGG/h-BN-OH-coated CF with varying wt% (2 and 4 wt%) showed significant improvement in CA of 114° and 129°, respectively, confirming the synergistic effect of each counterpart, which reduced the interaction between the water droplet and the CF by acting as a barrier. As a result, water droplets were repelled by the coated fabric and appeared in an almost ball-like shape, confirming their hydrophobic responses.

3.3. Mechanical properties and reinforcement mechanism

The mechanical properties of functionalized green and white graphene reinforced cotton fabric composites are crucial for evaluating their practical applicability and binding adhesion. Therefore, tensile tests were performed to examine the mechanical performance of untreated CF and CF treated individually or synergistically with the aforementioned reinforcements. The corresponding stress–strain curves, along with comparative bar plots summarizing fracture tensile strength and toughness, are shown in Fig. 3b and c, respectively. To optimize the coating composition, the hybrid content of AGG and h-BN-OH was varied. The resulting tensile properties are presented in Fig. 3b. Notably, AGG and h-BN-OH coated CF at 4 wt% exhibited significant improvements in fracture tensile strength (~170.5%), Young's modulus (~99.66%), toughness (~246.4%), and fracture strain (~12.63%) compared to pristine CF, indicating strong binding adhesion between the functionalized nanosheets and cellulose fibers. The enhancement is higher than that observed for individually h-BN-OH-coated CF, highlighting the importance of synergistic reinforcement through homogeneous dispersion and uniform coating. The mechanical reinforcement found in the coated fabrics primarily arises from modifications to the inter-fiber interface rather than from intrinsic strengthening of individual cellulose fibers. The introduction of amine-functionalized green graphene (AGG) forms a conformal 2D interfacial network over fiber surfaces, enabling strong H-bonding interactions between nitrogen-containing groups in DETA-functionalized biochar and cellulose –OH groups, along with complementary interactions with hydroxyl-functionalized h-BN-OH (Scheme 1a). Electrostatic interactions, supported by zeta potential measurements, further improve dispersion and coating uniformity. Such enhanced interfacial compatibility promotes efficient mechanical load transfer while minimizing stress concentration points within the fiber assembly, thereby strengthening the overall mechanical integrity of the coated fabrics [29]. Further investigation of AGG content (Fig. 3d and e) revealed that AGG-coated CF at 4 wt%

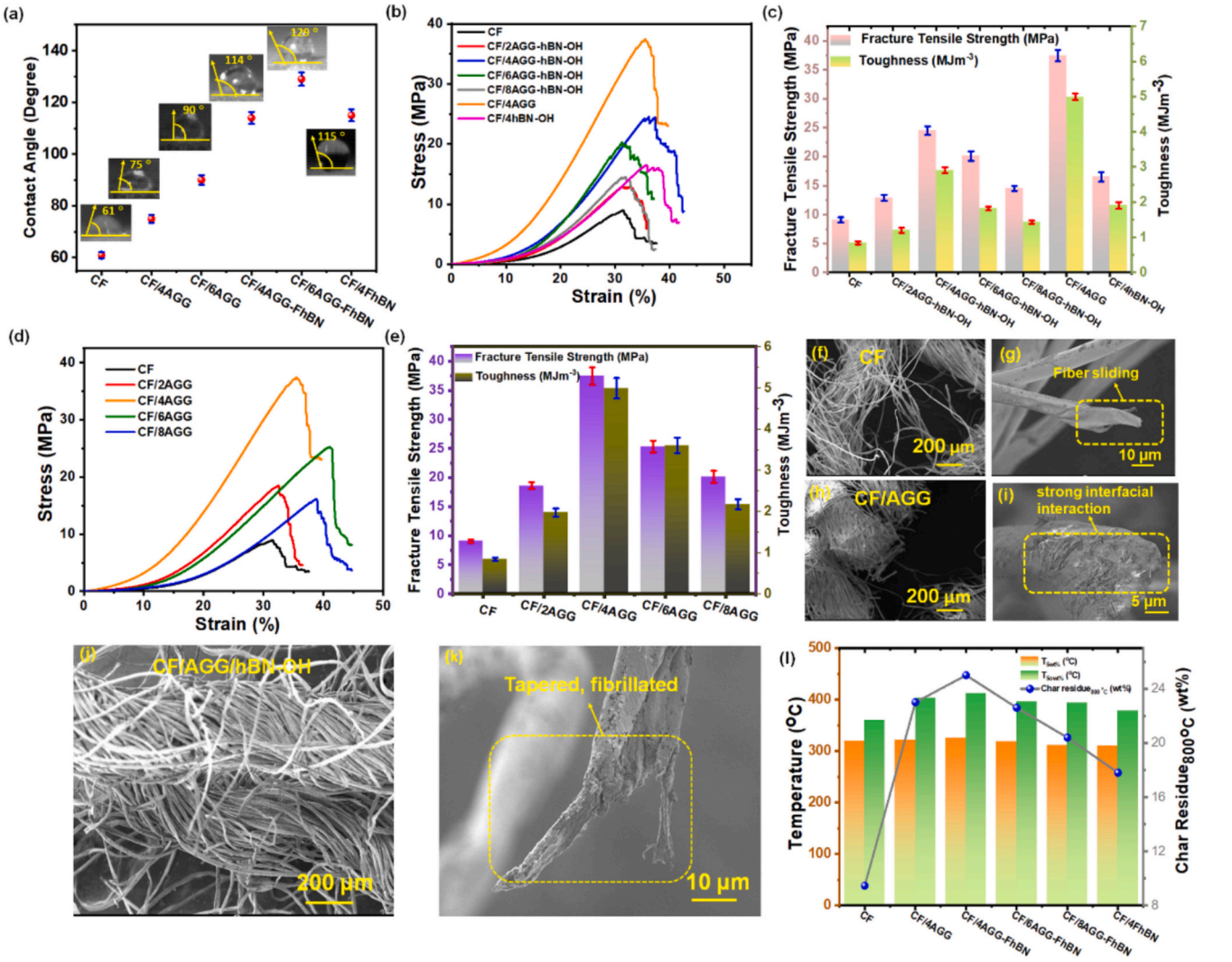

Fig. 3. a) Wettability behavior of pristine CF, individual AGG(or hBN-OH)-coated CF and AGG-hBN-OH coated CF with varying wt% (4 and 6 wt%), Stress-strain curves of b) Pristine CF and individually coating of AGG and hBN-OH (4 wt%) on CF and their hybrids with varying wt% (2, 4, 6 and 8 wt%) coating on CFs and c) the corresponding comparative bar plots of fracture tensile strength and toughness, error bars represent the standard deviation obtained from at least five independent tensile measurements. d) Stress-strain curves for pristine CF and varying wt% of AGG (2, 4, 6 and 8 wt%) coating on CFs and e) the corresponding comparative bar plots of fracture tensile strength and toughness, error bars represent the standard deviation obtained from at least five independent tensile measurements. Low and high magnification SEM images of tensile fracture morphologies of (f, g) pristine CF, (h,i) AGG coated CF (4 wt%) and (j, k) AGG-hBN-OH coated CF (4 wt%). l) the comparative bar plots of thermal degradation temperature variations at $T_{5wt\%}$, $T_{50wt\%}$ and variations of char residue left at 800 °C determined from TGA of pristine CF, and individually coating of AGG and hBN-OH (4 wt%) on CF and their hybrids with varying wt% (2, 4, 6 and 8 wt%) coating on CFs.

exhibited the highest fracture tensile strength (~313%), Young's modulus (~145.73%), and toughness (~494.5%), exceeding those of the hybrid-coated fabrics. This behavior suggests comparatively stronger interfacial interactions between the –NH_2 (or –NH) groups of functionalized biochar and the –OH groups of cellulose, resulting in more efficient stress transfer and improved strain accommodation.

The corresponding fracture morphologies of coated and uncoated CFs provide a clear mechanism for the improved tensile strength and toughness (Fig. 3f-k and Fig. S5). The flexible, defect-rich 2D structure of AGG enables the coating to accommodate deformation while maintaining interfacial contact, thereby improving tensile strength and toughness through enhanced strain accommodation and progressive failure. The corresponding fracture morphologies (Fig. 3h, i & Fig. S5a) further support this mechanism, showing compact yarn bundles, reduced fiber pull-out, and blunted, plastically deformed fiber ends, indicating delayed crack occurrence and effective stress redistribution compared to pristine CF. Upon incorporation of h-BN-OH nanosheets, additional interfacial reinforcement is introduced; however, due to h-BN-OH's higher intrinsic stiffness, the hybrid interphase becomes mechanically heterogeneous. The coexistence of flexible AGG domains and rigid h-BN-OH nanosheets introduces localized stiffness contrast, modifying load-transfer pathways and leading to partial stress localization during deformation (Fig. 3j, k & Fig. S5b). Consequently, the AGG/h-BN-OH-coated fabric maintains progressive, non-brittle failure characteristics. However, it exhibits partial fiber pull-out and tapered, fibrillated fracture features (Fig. 3k), consistent with localized interfacial debonding and reduced strain accommodation compared to AGG-only coated fabric. On the contrary, CFs typically fail through inter-fiber sliding and debonding due to limited load transfer between adjacent yarns (Fig. 3f, g). Although several approaches have been reported to improve the mechanical performance of cotton fabrics [30,31], the use of sustainably derived functionalized biochar and h-BN provides an environmentally favorable route to scalable fabrication. Overall, the mechanical performance of the coated fabrics is governed by interfacial bonding and stress redistribution mechanisms rather than coating thickness alone, with AGG primarily optimizing strain accommodation

and the AGG/h-BN-OH system enabling multifunctional performance, particularly enhanced flame retardancy.

3.4. Thermal stability and flame-retardant performance

To understand thermal stability and degradation behaviors of untreated CF and coated CF, TGA was carried out under N_2 atmosphere, as illustrated in Fig. 3l and Fig. S6. It is observed that all the treated cotton fabrics showed higher thermal stability in the entire temperature range compared to the untreated CF. The comparative bar plots of initial degradation temperature (i.e., at 5 wt% weight loss: $T_{5wt\%}$), 50 wt% weight loss temperature ($T_{50wt\%}$) and char residue left at 800 °C for all the fabrics, were presented in Fig. 3l. Interestingly, it is found that CF/4AGG-hBN-OH exhibited maximum thermal stability at both $T_{5wt\%}$ and $T_{50wt\%}$ owing to the synergistic effect of homogeneously distributed AGG and hBN-OH in CF. However, individual AGG-coated CF showed good thermal stability, but still lower compared to the previous one, suggesting the importance of employing both coatings on CF. Moreover, it is obvious that CF/4AGG-hBN-OH showed higher char residue compared to the individual decoration and even pristine CF, suggesting that the covered functionalized green graphene and h-BN can preclude the thermal degradation process of CF. Also, the coating process assists in dissipating the external heat conduction toward the CF through absorbing a part of the heat [25].

Improving the flame retardancy of CF is essential for its practical applications across various sectors. Infrared thermography was initially employed as an auxiliary technique to visualize heat propagation and provide qualitative insight into the thermal shielding behavior of the fabrics. A vertical flame testing setup combined with a thermal camera enabled monitoring of the time-dependent surface temperature during combustion. It should be noted that parameters such as heat propagation time are presented here as supportive indicators rather than primary fire-performance metrics. Fig. 4(a-c) illustrates the temperature-time profile of AGG-hBN-OH coated CF, AGG-coated CF, and pristine CF, and their time-dependent photographs during the flame test are shown in Fig. 4(d-h) and Figs. S7 and S8. It is observed that uncoated CF (Fig. 4c, Fig. S8 and Supporting Video 1) burns immediately, within 10 s, and shows almost 90% weight loss after burning. The propagation time of heat transfer from point zones 2, 4, 6, and 8 to points zone 1, 3, 5, and 7 is much shorter (~ 1.8 s), as evident from the corresponding temperature-time profile plot (Fig. 4c), suggesting that untreated CF is highly combustible, as expected. Interestingly, AGG/h-BN-OH- coated CF (Fig. 4a) showed significantly longer time (almost 16 s) for heat propagation between the mentioned corresponding zones, revealing pronounced inhibition of heat propagation by AGG and h-BN-OH, which was synergistically coated on CF. As a result, such treated CF showed remarkably decreased heat transfer time (~32 s) with almost 37% weight loss (Fig. 4h), demonstrating enhanced thermal shielding. The enhanced thermal shielding effect is associated with improved thermal stability, as the formation of a protective char layer effectively delays heat transfer and suppresses thermal degradation. The homogeneous dispersion of AGG and h-BN-OH in CF assists the formation of a char layer on the cotton surface and precludes the contact between combustible gases and the flame front. The lamellar structure of both h-BN-OH and AGG inhibits the degradation of cellulose chains, and their charred layer acts as a barrier to block the diffusion of oxygen and the volatilization of combustible gases. Especially, due to the promising thermal stability and non-combustible nature of h-BN-OH, the coated cotton fabric demonstrated a remarkably lower rate of heat transfer during the infrared thermography test [32]. Also, the functionalization of GG by DETA, which is stable under fire, not only acts as a heat absorber but also reduces heat transfer by forming a char layer [25,33]. In contrast, The AGG-coated CF (Fig. 4b) shows intermediate behavior, with heat propagation occurring within ~4.5 s and a total heat transfer time of ~16 s (Fig. S7), highlighting the synergistic role of AGG and h-BN-OH in improving thermal resistance. The corresponding video file for AGG and h-BN-OH-coated CF is depicted in Supporting Video 2. To further identify the extent of char layer on coated and uncoated CFs, SEM was conducted, as presented in Fig. 4 (i, j). Notably, in the case of AGG/h-BN-OH-coated CF (Fig. 4i), a dense char layer is formed on the surface of CF owing to the generation of thermo-stable products from the combustion of homogeneously dispersed AGG and h-BN-OH during the test. Also, at high temperatures, cellulose itself was carbonized to provide water, CO_2, and char residue. In the meantime, nonflammable volatile (N_2,NH_3) was also produced, which is found to dilute oxygen and flammable volatiles, effectively suppressing combustion. Owing to such a developed dense char layer, the corresponding surface roughness is increased, and as a result, the internal fibers of CF were protected against flame and heat. On the contrary, the surface of CF (Fig. 4j) after burning is smooth, resulting in rapid flame propagation. Furthermore, the residue of pristine CF was loose and brittle, while that of coated CFs was more compacted. Additionally, AGG-coated CF (Fig. S9) is also found to form a thin char layer after combustion, leading to comparatively lower roughness on the surface. Therefore, it showed moderate flame propagation response, as evident from earlier findings. Hence, we can depict that the synergistic coating of functionalized green graphene and white graphene on cotton fabric achieved pronounced flame-retardancy. Similar behavior is observed for AGG-h-BN-OH–coated jute fibers, which exhibit self-extinguishing characteristics, whereas pristine jute burns instantly (Supporting Videos 3 and 4).

To provide quantitative validation of the flame-retardant behavior of the coated cotton fabrics, the limiting oxygen index (LOI) measurements of pristine and coated CF samples are further presented in Fig. 4k. The pristine CF exhibited a low LOI of about 19.1%, reflecting its high flammability. Upon AGG coating, the LOI increased significantly to about 25.7%, indicating improved resistance to sustained combustion. Notably, the AGG/hBN-OH coated CF exhibited a further enhancement in LOI to about 30.2%, reflecting substantial improvement in flame retardancy. The increase of ~11% in absolute LOI value compared to pristine CF confirms the synergistic effect of AGG and hBN-OH in suppressing combustion. The improved flame-retardant behavior can be due to the formation of a thermally stable protective barrier layer, which reduces heat transfer and restricts oxygen diffusion to the underlying substrate, reaffirming the effectiveness of the surface modification strategy [34].

The flame-retardant behavior of the pristine and coated fabrics was also studied using a vertical flame test following a modified ASTM D6413 method. Upon ignition and removal of the ignition source, the pristine CF exhibited rapid flame propagation and noticeable dripping due to slight fragment fall-off, suggesting poor resistance to flame spread and reduced structural stability during combustion. On the contrary, both AGG and AGG/hBN-OH coated fabrics showed significantly slower flame propagation, demonstrating improved resistance to combustion spread, consistent with previous findings. Notably, AGG/hBN-OH coated fabric exhibited a pronounced shorter char length of 2.4 cm compared to 5.0 cm for AGG-coated fabric, indicating substantial reduction in flame propagation distance. Notably, no dripping behavior was observed for the coated fabrics. In contrast, pristine CF showed dripping during combustion, suggesting enhanced structural integrity and the formation of a cohesive protective layer. Despite the absence of complete self-extinguishing behavior, the coated fabrics exhibited slower flame propagation and reduced char length, indicating a moderate improvement in flame-retardant properties. Table S1 summarizes the vertical flame test results. The enhanced flame-retardant performance is primarily attributed to a condensed-phase mechanism in which biochar-derived AGG promotes char formation, which acts as a barrier to heat transfer, oxygen diffusion, and volatile release. The incorporation of h-BN-OH further improves thermal stability and barrier properties by creating a tortuous pathway that suppresses heat and mass transfer [34,35]. This synergistic effect results in a compact and protective char layer (as evident from Fig. 4i), thereby reducing flame spread and improving fire resistance compared to pristine CF. This

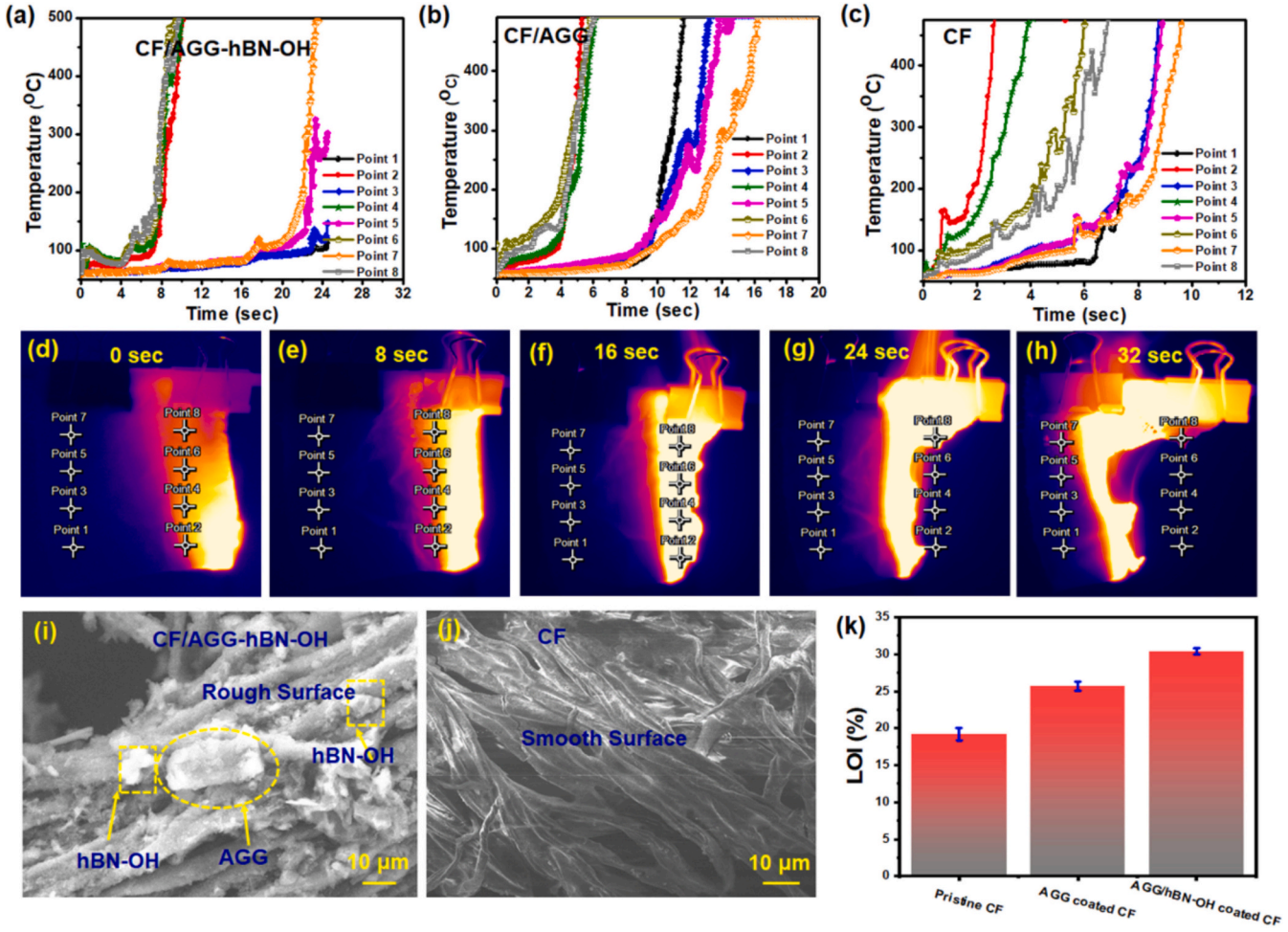

Fig. 4. Flame-retardant responses of coated and uncoated CFs: Temperature propagation behavior with time for a) AGG and h-BN-OH coated CF, b) AGG coated CF, and c) pristine CFs; Infrared thermal images of AGG/hBN-OH coated CF during direct flame exposure at (d) 0 s, (e) 8 s, (f) 16 s, (g) 24 s and (h) 32 s. The AGG/hBN-OH coated CF showed delayed heat propagation, indicating improved flame-retardant response; After combustion SEM images of i) AGG/h-BN-OH-coated CFs and j) pristine CFs; Comparison of limiting oxygen index (LOI) values of pristine CF, AGG coated CF and AGG/hBN-OH coated CF fabrics, determined according to modified ASTM D2863, demonstrating enhanced flame retardancy after AGG and AGG/hBN-OH surface modification.

mechanism is further supported by the reduced heat flux and heat transfer coefficient obtained from M–Z interferometry (discussed later), as well as the delayed heat propagation observed in infrared thermography (Fig. 4a-h). A possible secondary gas-phase contribution may arise from nitrogen-containing groups introduced via DETA, which could interfere with flame-propagating radicals or dilute combustible gases; however, this effect is considered minor due to the lack of direct evidence. Notably, the formation of a compact and thermally stable char layer promotes rapid heat dissipation, thereby suppressing smoldering combustion after flame extinction; hence, the after-glow time is recorded as 0 s. Moreover, the flame colors provide further insight into the burning behavior. Pristine cotton fabric (CF), the cellulose fibers are rapidly consumed during burning, resulting in yellow bright flame, therefore, after-glow is recorded as 0 s. The yellow-orange and reddish-orange flames found for AGG and AGG/hBN-OH coated CF reflects partial and incomplete combustion, respectively, are consistent with the reduced flame intensity and enhanced flame-retardant performance of the coated samples.

To further elucidate the flame-retardant mechanism beyond conventional burning observations, Mach–Zehnder interferometric (MZI) analysis was employed to visualize heat flow and thermal gradients during controlled thermal exposure. The thermal field and convective response of coated and uncoated CFs under uniform bottom heating were examined by MZI studies [36,37]. The MZI setup used to visualize the convective thermal field above the heated specimens is shown in Fig. S10, and the detailed methodology is provided in the Experimental Section of Supporting Information. Heat transfer experiments were conducted for three fabric variants—pristine CF, h-BN–OH-coated CF, and AGG–h-BN–OH-coated CF—for a duration of 880 s to assess their flame-retardant response. The subsequent changes in the surface temperature are presented in Fig. 5a and Fig. S11a. The pristine CF showed a sharp and almost linear temperature ascent, reaching 77.6 ± 0.9 °C at the end of 880 s. In contrast, h-BN–OH-coated CF showed 74 ± 0.9 °C, while the AGG–h-BN–OH-coated CF depicted the lowest surface temperature of 70 ± 1 °C. The comparatively lower temperature increment is found for the coated fabrics revealing enhanced thermal insulation and suppressed heat flow, in accordance with their enhanced flame-retardant response. The h-BN–OH coating acts as a heat-resistant ceramic barrier that accelerates lateral heat conduction and decreases the surface temperature gradient, while the AGG layer further strengthens this effect by forming a porous carbonaceous structure that captures air and enhances interfacial thermal resistance [37–39]. Subsequently, the coated fabrics demonstrate lower surface temperatures than the pristine CF, reaffirming their effectiveness in confining heat dissipation under uniform heating.

Fig. 5b depicts the 3D interferogram taken at the initial state, while Figs. 5c, d and Fig. S11b represent the 3D interferograms captured for pristine CFs at a surface temperature of 70 °C at the end of 710 s and for

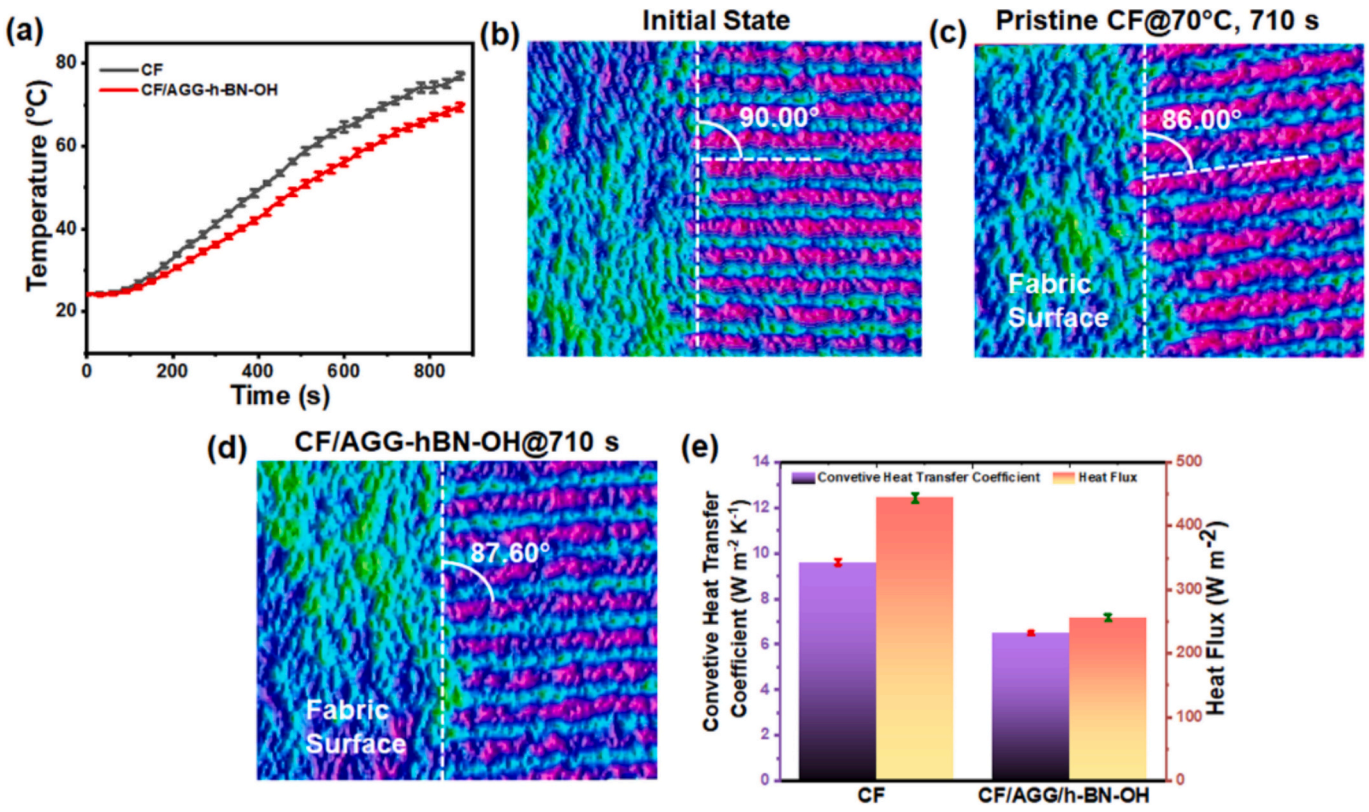

Fig. 5. Mach–Zehnder interferometric analyses of pristine CF and AGG-h-BN-OH hybrid coated CFs under uniform bottom heating: a) Surface temperature–time profiles of pristine CF and AGG-hBN-OH hybrid coated CFs; Mach–Zehnder interferograms of b) initial state, c) pristine CF at 70 °C at 710 s and d) AGG-h-BN-OH coated CF at 710 s; e) Comparison of convective heat-transfer coefficient (h) and heat flux (q) for pristine CF and AGG-h-BN-OH coated CF.

CF/AGG–h-BN-OH and CF/h-BN-OH at the end of 710 s, respectively. Initially, all samples exhibit straight, parallel fringes, suggesting a uniform refractive index distribution in the ambient air. With continuous heating, fringe bending takes place near the surface owing to air density gradients, indicating the temperature and convective flow fields above each specimen. The pristine CF depicts the largest fringe bending (86 ± 0.1°), related to a steeper temperature gradient and stronger convective heat transfer. In contrary, CF/h-BN–OH (87.1 ± 0.1°) and CF/AGG–h-BN–OH (87.6 ± 0.1°) exhibit smaller fringe deflections in comparison to the initial state, implying weaker refractive index gradients and delayed convective heat loss. These smaller deviations reflect that both surface heating and heat dissipation to the surrounding air are considerably reduced by the coatings.

The convective heat transfer coefficient (h) and heat flux (q), evaluated using Naylor's formulation (Fig. 5e and Fig. S11c), further validate this effect. Related to pristine CF (h = 9.6 ± 0.13 W m^{-2} K^{-1}, q = 444 ± 7 W m^{-2}), the h-BN–OH-coated and AGG–h-BN–OH-coated fabrics show reduced values of h = 7.4 ± 0.15 W m^{-2} K^{-1} and 6.5 ± 0.08 W m^{-2} K^{-1}, and q = 321 ± 10 W m^{-2} and 256 ± 5 W m^{-2}, respectively. Although the absolute reduction in h is about 3 W m^{-2} K^{-1}, it signifies a substantial ~30% decrease compared to pristine CF, confirming a noticeable suppression of surface-to-air heat transfer. The reduction in both h and q arises from the synergistic thermal barrier mechanism of the coatings: the h-BN–OH layer offers efficient in-plane heat spreading through a stable ceramic interface, while the AGG layer promotes interfacial resistance and restricts through-thickness conduction [37–39]. Together, they efficiently inhibit both conductive and convective heat transfer, resulting in significantly lower heat flux. The interferometric findings validate the surface-temperature analysis, quantitatively corroborating the superior thermal-shielding performance and improved flame-retardant behavior of the coatings. Among them, the AGG–h-BN–OH composite exhibits the highest thermal resistance, owing to the synergistic combination of h-BN–OH's lateral heat dissipation and AGG's char-stabilizing effect.

The evaluation of flame-retardant performance based solely on LOI and vertical burning tests is limited, as high LOI values do not necessarily reflect real fire behavior. Although cone calorimetry remains a benchmark technique, the combined use of infrared thermography, LOI, vertical burning, M–Z interferometry provides a comprehensive and mechanistically supported evaluation of flame-retardant behavior, capturing both macroscopic flammability characteristics and underlying heat transfer suppression mechanisms, particularly useful for surface-engineered textile systems. In future work, detailed cone calorimetry studies will be conducted to enable direct quantification of heat release parameters and to provide additional validation of the present findings.

3.5. *Water-immersion stability and antibacterial performance*

To evaluate the water-immersion stability of the AGG and h-BN–OH coatings on CFs, tensile tests, contact angle (CA) measurements, heat transfer behavior and flame-retardant analyses were performed after 10 and 20 repeated water-immersion and drying cycles. The initial evaluation of coating stability under mild aqueous conditions has been carried out rather than standardized laundering durability, as the system is a binder-free coating system. The mechanical behavior of pristine CFs, freshly coated CFs, and washed samples is presented in Fig. S12a and Table S2. After 10 repeated water-immersion and drying cycles, the coated CFs retained 87% of their fracture tensile strength and 70% of their toughness, demonstrating the robust interfacial adhesion of the AGG/h-BN–OH coating through hydrogen bonding and electrostatic interactions. Even after 20 repeated water-immersion and drying cycles, 67% of the tensile strength and 48% of the toughness were preserved, highlighting the coating's long-term mechanical stability. The water repellence response also remained largely unaffected, even after

repetitive washing. The coated CFs exhibited contact angles of ~121° and ~ 108° after 10 and 20 repeated water-immersion and drying cycles, respectively (Fig. S12b), preserving excellent hydrophobicity. The consistently high CA values and nearly spherical droplet reveal the homogeneous distribution and strong adhesion of AGG and h-BN–OH with CF are responsible for effectively impeding water permeation. The temperature–time profiles and corresponding infrared images (Fig. S12c,d) further demonstrate the stability of the coating under repeated aqueous exposure. After 10 repeated water-immersion and drying cycles, the coated CFs exhibited heat propagation of ~12 s between designated zones and a total heat transfer duration of ~28 s, comparable to that of the unwashed coated sample (~32 s). This behavior suggests that the lamellar AGG/h-BN–OH structure continues to act as an effective thermal barrier by limiting heat transfer and restricting the diffusion of oxygen and volatile combustible species. Even after 20 repeated water-immersion and drying cycles, the coated CFs preserved a heat propagation time of ~8.5 s to reach the prementioned zones and a heat transfer duration of ~20 s, indicating sustained, though slightly reduced, thermal barrier performance. The coated CF exhibited LOI values of 27.5% and 24.3% after 10 and 20 repeated water-immersion and drying cycles, respectively, from an initial value of 30.2%, demonstrating appreciable retention of flame-retardant performance under repeated aqueous exposure, consistent with the previous findings. The overall performance, including fracture tensile strength, toughness, contact angle, heat transfer time and LOI% before and after 10 and 20 repeated water-immersion and drying cycles of CF/4AGG-hBN-OH, is summarized in Table 1. Collectively, these results suggest that the synergistic incorporation of "green graphene" (AGG) and "white graphene" (h-BN–OH) offers good stability under repeated water-immersion and drying conditions, allowing the coated CFs to largely retain their mechanical integrity, surface hydrophobicity and flame-retardant characteristics.

To assess the antibacterial effectiveness of the developed coatings, Gram-positive (*S. aureus*) and Gram-negative (*E. coli*) bacteria were separately cultured on pristine CFs and CFs coated individually with AGG (4 wt%) AGG/h-BN–OH hybrid (4 wt%) using the agar diffusion assay (Fig. 6a-f). After incubation for 24 h, antibacterial activity was evaluated by optical photographs of the cultured plates. Fig. 6a-c depicts the inhibition of *S. aureus*, while Fig. 6d-f resembles to *E. coli*. Among all compositions, the CF coated with 4 wt% AGG/h-BN–OH showed the most pronounced antibacterial activity, demonstrating inhibition zones of approximately 12.5 mm (Fig. 6c) against *S. aureus* and 15.5 mm against *E. coli* (Fig. 6f). This superior performance is due to the stronger interfacial interaction between AGG, h-BN–OH, and the cellulose fibers via hydrogen bonding—especially, between the hydroxyl groups of h-BN–OH and the amine groups of AGG with the –OH functionalities of cellulose. On the contrary, AGG-coated CF exhibited an inhibition zone of ~8.4 mm against *S. aureus* (Fig. 6b) and 9.7 mm against *E. coli* (Fig. 6e). Notably, in either case, pristine CF did not exhibit any detectable inhibition zone, confirming the absence of inherent antibacterial activity, rather the formation of biofilm over CF. Importantly, the functional groups interact with bacterial cell membranes, leading to membrane disruption and reduced bacterial viability in the coated fabrics [40]. These findings indicate that the 4 wt% AGG/h-BN–OH hybrid effectively inhibit biofilm formation and bacterial proliferation without using any cytotoxic metallic nanoparticles. Therefore, the optimized AGG/h-BN–OH coating provides sustainable and is a promising candidate to potent biological protection for applications in safety and protective textiles.

Fig. 6(g–o) depicts the quantitative antibacterial performance of control (without any fabric), pristine CF, CF/AGG, and CF/AGG/hBN-OH against *Escherichia coli* and *Staphylococcus aureus* after 24 h incubation. The control plates showed dense bacterial growth, confirming normal bacterial proliferation under the test conditions, whereas pristine CF exhibited only minimal antibacterial activity (Figs. 6g, h, k, l). In contrast, AGG-coated CF resulted in a clear reduction in colony formation in either case (Figs. 6i and m), indicating improved antibacterial activity. The CF/AGG/hBN-OH sample demonstrated the lowest colony density (Figs. 6j and n) and the highest bacterial reduction percentage (Fig. 6o), suggesting a synergistic effect of AGG and hydroxyl-functionalized hBN. The enhanced antibacterial performance is attributed to the presence of surface functional groups that interact with bacterial cell membranes, causing membrane disruption and reduced bacterial viability. A relatively higher inhibition was observed against *E. coli* compared to *S. aureus*, which may be associated with differences in bacterial cell wall structure and susceptibility to surface-induced damage. The quantitative bacterial reduction (%) results are in consistent with inhibition zone results, indicating effective antibacterial functionality of the hybrid coating.

3.6. Comparison with reported multifunctional cotton fabric coatings

In order to investigate the overall efficiency of AGG/hBN-OH-coated CF with reported coatings of CFs [25,41–49], we compared all the properties as depicted in Fig. 7. Notably, our engineered fabric exhibits superior mechanical strength, hydrophobicity, thermal stability, and an increased fire propagation time in comparison to reported CFs. Together, these findings emphasize the efficacy of employing sustainable AGG/hBN-OH hybrid coating in developing multifunctional cotton-based textiles. The present coating technique represents a fabric-level surface modification, in which mechanical reinforcement (as discussed earlier) is generated by improved inter-fiber adhesion and load transfer rather than by the intrinsic strengthening of individual cellulose fibers. The low coating add-on (2–6 wt%), facile dip–dry processing, and sustainable and cost-effective source of raw materials are compatible with conventional textile finishing routes, suggesting potential scalability. Compared with many binder-assisted or APP-based flame-retardant coatings, which require relatively high add-on levels to achieve effective flame resistance [43,47,50], the present system achieves simultaneous mechanical reinforcement, hydrophobicity, flame retardancy and antibacterial effectiveness through interfacial engineering. Water-immersion stability tests indicate that the coating maintains functional performance after 20 repeated water immersion and drying cycles, confirming good coating stability.

The wearability of the coated fabrics is an important consideration for practical applications. Optical microscope analysis reveals that the coating forms a thin and conformal layer on the fiber surface, leading to an increase in fiber diameter [25.579 μm from 12.875 μm (Fig. 2h, i)] while preserving the inter-fiber porous structure as evident from the corresponding SEM images (Fig. S13). The open inter-fiber structure further supports minimal pore occlusion. This indicates that the coating does not block the fabric pores, thereby maintaining air permeability,

Table 1
Retention of tensile properties, water contact angle, heat transfer response and flame-retardant performance of coated cotton fabric (CF/4AGG-hBN-OH) after repeated water-immersion and drying cycles (0, 10, and 20 cycles).

Sample	Fracture tensile strength (MPa)	Toughness (MJm^{-3})	Contact angle (°)	Heat transfer time (s)	LOI (%)
CF/4AGG-hBN-OH@0C[a]	24.513 ± 0.84	2.91 ± 0.74	129 ± 2.0	32 ± 1.0	30.2 ± 0.41
CF/4AGG-hBN-OH@10C[a]	21.37 ± 1.1	2.04 ± 0.92	121 ± 3.0	28 ± 1.5	27.5 ± 0.49
CF/4AGG-hBN-OH@20C[a]	16.35 ± 0.92	1.38 ± 0.73	108 ± 2.0	20 ± 1.7	24.3 ± 0.53

[a] C denotes number of water-immersion and drying cycles.

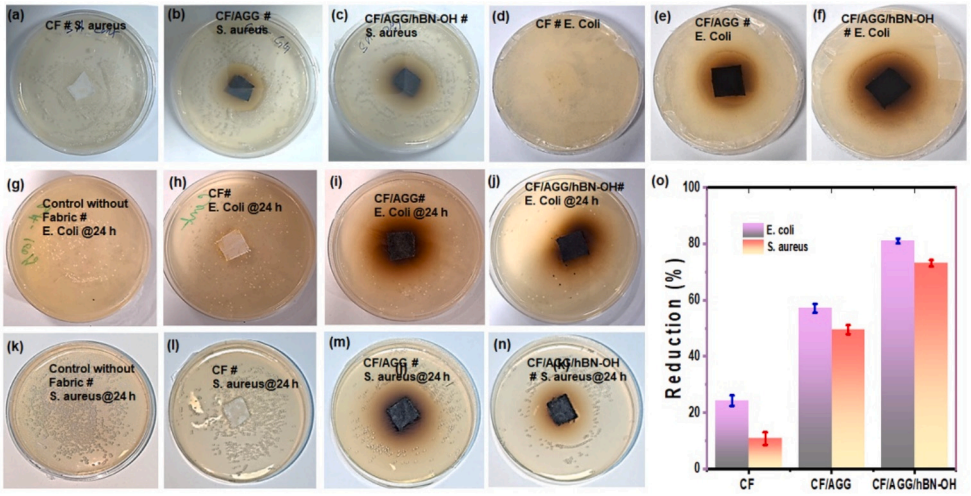

Fig. 6. Antibacterial effect of pristine CFs and varying concentrations of AGG and h-BN-OH-coated CFs against *S. aureus* and *E. coli*: (a-f) Agar diffusion assay images showing antibacterial activity of pristine CF, AGG-coated CF, and AGG/h-BN-OH-coated CFs against *E. coli* and *S. aureus* after 24 h incubation. No inhibition zones are observed for pristine CF for both *S. aureus* and *E. coli*, whereas clear zones are visible around the coated CFs; (g–j) Colony-count based quantitative bacterial reduction against *E. coli* after 24 h incubation; (k–n) Colony-count based quantitative bacterial reduction against *S. aureus* after 24 h incubation, (o) Corresponding bacterial reduction percentage (mean ± SD, $n = 3$).

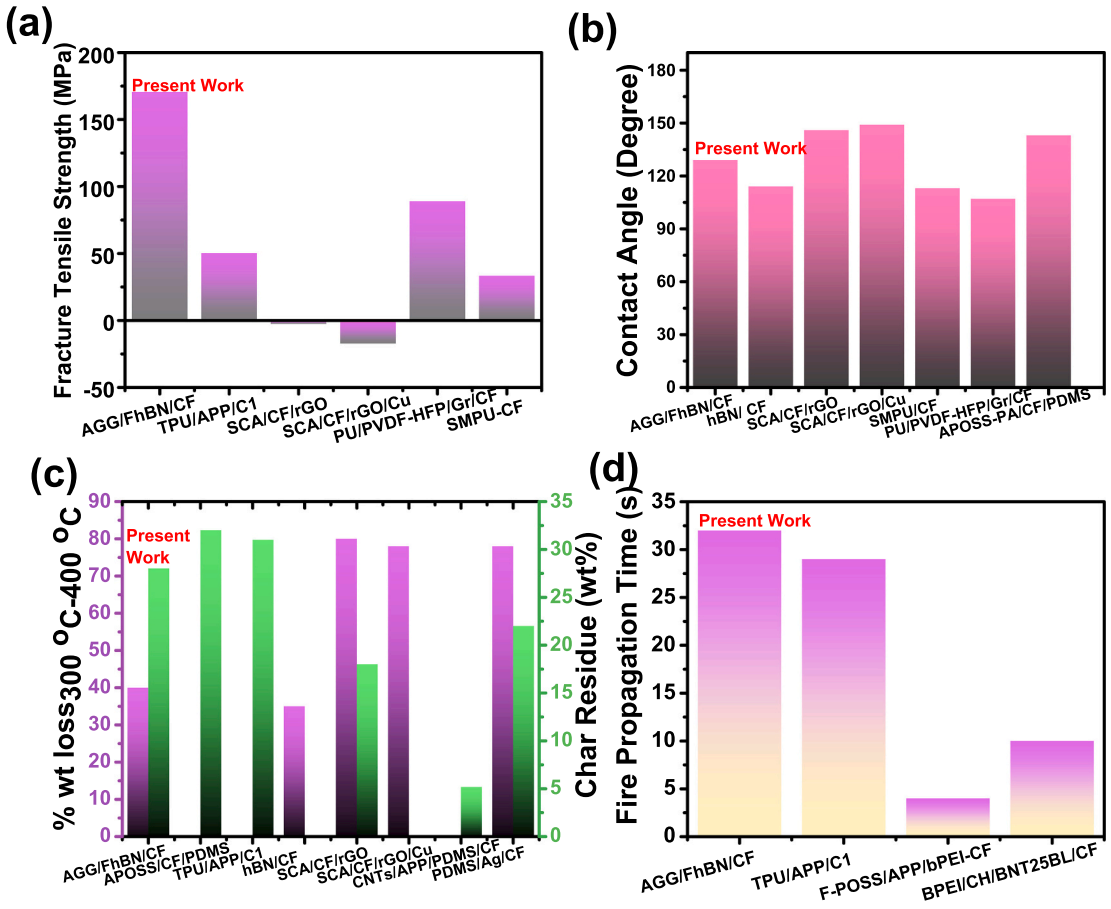

Fig. 7. Relative performance of AGG/hBN-OH coated cotton fabric with reported fabric coatings: (a) Fracture tensile strength, (b) water contact angle, (c) thermal stability, and (d) fire propagation time. Our designed fabric demonstrates superior durability, hydrophobicity, thermal stability, and flame retardancy.

which is essential for breathability and comfort. In addition, the thin and conformal coating ensures that the intrinsic flexibility of the fabric is preserved without noticeable stiffness during handling, indicating minimal impact on hand feel (Fig. S14 and Supporting Video 5). he rubbing fastness of the coated fabrics is qualitatively inferred to be satisfactory, as the functional coating exhibits good adhesion to the fiber surface, evidenced by the retention of mechanical, hydrophobic, and flame-retardant properties after repeated water immersion–drying

cycles (Fig. S12 and Table 1). This indicates reasonable resistance to mechanical abrasion and durability of the coating layer. In addition, a qualitative rubbing test was performed by manually rubbing the coated fabric against a clean glass substrate. No visible transfer or leaching of the coating was observed on the glass surface, indicating good adhesion and resistance to mechanical abrasion (Fig. S15 and Supporting Video 6). Although detailed quantitative evaluation of air permeability and rubbing fastness was beyond the scope of the present study, the structural integrity and performance retention suggest that the coated fabrics maintain acceptable wearability, which will be systematically investigated in future work. The developed system is positioned as a sustainable multifunctional coating strategy for functional textiles rather than a fully optimized commercial finishing technology.

3.7. Molecular dynamics simulation for flame-retardant mechanism

To investigate the morphological evolution during reactive MD simulations, the atomic structures of pristine and coated cellulose systems were examined, as displayed in Fig. 8a–f. All reactive MD simulations were performed under identical thermal conditions, with equilibration at 300 K followed by heating to 2500 K over 100 ps, to ensure consistent comparative analysis among the different systems. These snapshots denote the initial structures and the corresponding molecular dynamics (MD) configurations at an early stage of molecular fragmentation for three systems: pristine cellulose, cellulose coated with h-BN–OH, and cellulose coated with a dual layer of AGG and h-BN–OH. The images allow a direct assessment of the early-stage structural integrity and molecular fragmentation features at the atomistic scale. In all MD simulations, the onset of molecular fragmentation was associated with the appearance of CO- and CO_2-like fragments, serving as qualitative indicators of high-temperature bond cleavage. In the pristine cellulose system, these fragments appeared earlier, at approximately 12 ps. In contrast, the cellulose/h-BN– OH heterostructure exhibited a delayed onset, with molecular fragments appearing around 22 ps (Figs. 8b, d). This enhanced resistance to early-stage molecular fragmentation stems from the protective h-BN–OH layer, which acts as a structurally stable barrier, delaying the formation and migration of volatile fragments at the atomistic scale. Particularly, the introduction of an additional AGG interlayer between the cellulose and h-BN–OH (Figs. 8e, f) further enhanced resistance to molecular fragmentation. In this configuration, the appearance of CO- and CO_2-like fragments was further delayed (approximately 32 ps), indicating a delayed onset of molecular fragmentation under the simulated conditions. This synergistic improvement aligns with earlier findings on the thermal-shielding behavior of 2D materials [51,52]. While h-BN–OH offers chemical inertness and high structural stability, AGG contributes to enhanced interfacial cohesion and reduced molecular mobility within the composite. The combined architecture thus promotes enhanced structural confinement and reduced molecular mobility at the atomistic scale, delaying the onset and progression of early-stage molecular fragmentation under the simulated conditions. The reactive MD simulations of pristine CF and AGG/h-BN–OH–coated CFs (Supporting Videos 7 and 8) reproduce the same qualitative delay in early-stage molecular fragmentation trends observed experimentally.

The molecular evolution profiles presented in Fig. 8g–i, obtained from a quantitative post-processing analysis of the MD trajectories based

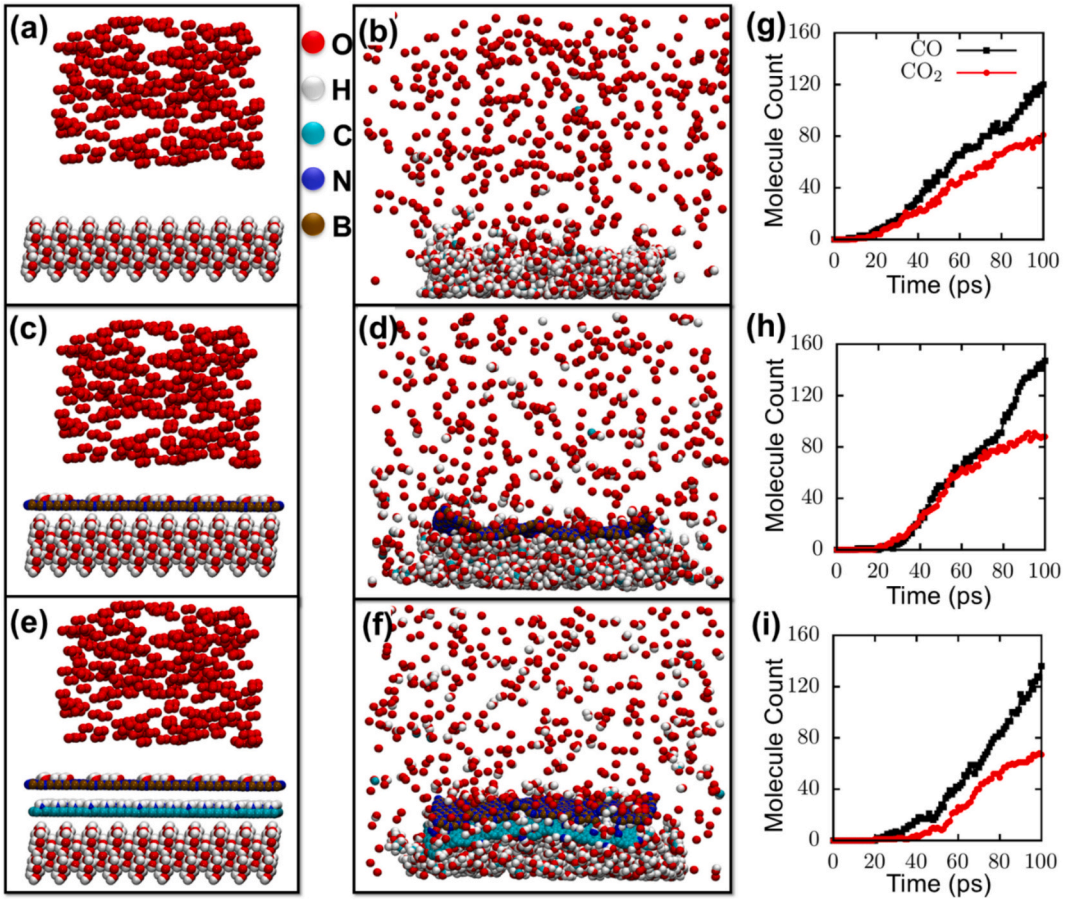

Fig. 8. Schematic illustration of the modeled systems in the presence of atomic oxygen: (a) pristine cellulose, (c) cellulose coated with hBN-OH, and (e) cellulose coated with AGG and hBN-OH at an early stage of the MD simulation; (b), (d), and (f) show the respective configurations at an early stage of molecular fragmentation. Number of CO- and CO_2-like fragments (black squares and red circles, respectively) formed over time during the reactive MD simulations of (g) pristine cellulose, (h) hBN-OH-coated cellulose, and (i) AGG/hBN-OH-coated cellulose.

on fragment connectivity, quantitatively describe the temporal evolution of molecular fragmentation in the simulated systems. In all systems, the number of CO-like fragments exceeds that of CO_2-like fragments, indicating a higher prevalence of partial bond cleavage events under the simulated conditions. The h-BN–OH–coated system (Fig. 8h) shows a similar overall trend to the pristine cellulose (Fig. 8g), but with reduced slopes and slower accumulation of CO- and CO_2-like fragments, indicating a delayed progression of molecular fragmentation under the simulated conditions. Upon the introduction of the AGG interlayer between cellulose and h-BN– OH, the generation of both CO and CO_2 becomes even less pronounced (Fig. 8i), aligned with the delayed onset of molecular fragmentation observed structurally. Under the simulated thermal environment, the graphene layer remains unaffected, without carbon release into detached molecular fragments, thereby not contributing to the formation of CO- or CO_2-like fragments. These atomistic trends are qualitatively consistent with the experimentally observed improvement in flame-retardant performance.

4. Conclusions

In the present work, multifunctional cotton fabrics were rationally designed through a sustainable hybrid-coating route using aminated green graphene (AGG) and hydroxylated hexagonal boron nitride (h-BN–OH). The two components develop a strong interfacial network via hydrogen bonding and electrostatic interactions, governing a simultaneous enhancement of textile performance. The resulting CFs revealed a unique combination of hydrophobicity, antibacterial activity, mechanical durability, and fire retardancy, mitigating various inherent drawbacks of conventional cotton textiles. The incorporation of AGG and hBN-OH not only enhanced the fracture strength (~171%), toughness (~246%) of the fabrics, and hydrophobicity (CA ~ 129°) remarkably, but also offered protection against microbial growth and fire hazards, and demonstrated prolonged water-immersion stability even after 20 washings. The combination of reduced char length, absence of melt dripping behavior, slower flame propagation, enhanced TGA char residue and improved LOI values collectively supports the improved flame-retardant behavior of AGG/hBN-OH coated fabric The MZI analysis suggests that the AGG–h-BN–OH-coated CF reveals the strongest thermal-shielding effect, with a prominent reduction of surface temperature, heat flux, and convective heat transfer compared to pristine CF. This superior performance originates from the combined action of the h-BN–OH ceramic barrier and AGG interlayer, which together hinder both conductive and convective heat dissipation. Comparative analyses also indicate that the hybrid-coated CFs surpassed single- component coatings and many previously reported textile modifications, highlighting the synergistic effect of graphene and h-BN in accomplishing multifunctionality. The MD simulations indicate that the dual-layer AGG/h-BN–OH coating promotes enhanced structural stability at the atomistic scale through synergistic physical shielding and reduced molecular mobility. The h-BN–OH layer contributes to structural confinement, while the AGG interlayer supports interfacial cohesion, collectively delaying the onset and progression of early-stage molecular fragmentation under the simulated conditions. These atomistic trends are qualitatively consistent with the experimentally observed improvement in flame-retardant performance. This unique technique provides a versatile, halogen-free, and environmentally friendly approach for developing next-generation smart textiles with potential applications in healthcare, protective clothing, filtration, and other high-performance *sec*tors. Moreover, it offers opportunities for further functionalization and scale-up toward commercially viable, durable, and sustainable cotton-based textiles.

CRediT authorship contribution statement

Moumita Kotal: Writing – review & editing, Writing – original draft, Validation, Methodology, Investigation, Formal analysis, Data curation, Conceptualization. **Guilherme da Silva Lopes Fabris:** Writing – original draft, Validation, Investigation, Formal analysis, Data curation. **Surbhi Slathia:** Formal analysis, Data curation. **Akbar Shanu:** Investigation, Formal analysis, Data curation. **Rakesh Das:** Formal analysis. **Bruno Ipaves:** Writing – review & editing, Formal analysis. **Marcelo Lopes Pereira Júnior:** Writing – review & editing, Data curation. **Bidush Das:** Resources. **Jayanta Bhattacharya:** Resources. **Sajith Vandana:** Writing – review & editing. **Douglas Soares Galvão:** Writing – review & editing, Validation. **Chandra Sekhar Tiwary:** Writing – review & editing, Supervision, Resources, Funding acquisition, Conceptualization.

Declaration of competing interest

The authors declare that they have no known competing financial interests or personal relationships that could have appeared to influence the work reported in this paper

Acknowledgements

M.K. and C.S.T. acknowledge the financial support from the National Technical Textiles Mission (NTTM), Government of India. G.S.L.F. acknowledges support from FAPESP process number #2024/03413-9. B.I. acknowledges support from CNPq and São Paulo Research Foundation (FAPESP) process numbers #194155/2025-0 and #2024/11016-0. M.L. P.J. acknowledges financial support from FAPDF (grant 001 93-00001807/2023-16), CNPq (grants 444921/2024-9 and 308222/2025-3), and CAPES (grant 88887.005164/2024-00). D.S.G. acknowledges the Center for Computing in Engineering and Sciences at Unicamp for financial support through the FAPESP/CEPID Grant #2013/08293-7. The authors thank the Coaraci Supercomputer Center for computer time (FAPESP grant #2019/17874-0). D. S. G. also acknowledges support from INEO/CNPq and FAPESP grant # 2025/27044-5. C.S.T. also acknowledges the AOARD (Asian Office of Aerospace Research and Development) grant no. (FA2386-21-1-4014), and naval research board for funding support. The authors thank Mr. Nitai Giri for his assistance with antibacterial studies.

Appendix A. Supplementary data

Supplementary data to this article can be found online at https://doi.org/10.1016/j.cej.2026.176668.

Data availability

Data will be made available on request.

References

[1] W. Li, Z. Yu, Y. Zhang, C. Lv, X. He, S. Wang, Z. Wang, b. He, S. Yuan, J. Xin, Y. Liu, T. Zhou, Z. Li, S.C. Tan, L. Wei, Scalable multifunctional MOFs-textiles via diazonium chemistry, Nat. Commun. 15 (2024) 5297.
[2] H. Ru, Y. Ma, Y. Jin, S. Xiang, S. Zhao, F. Fu, X. Liu, P.J. Dyson, Z. Fei, A facile strategy based on ionic liquids to modulate the antibacterial, flame-retardant, and sensing properties of cotton fabrics, Adv. Funct. Mater. 35 (2025) 2425093.
[3] Q. Qin, R. Guo, E. Ren, X. Lai, C. Cui, H. Xiao, M. Zhou, G. Yao, S. Jiang, J. Lan, Waste cotton fabric/zinc borate composite aerogel with excellent flame retardancy, ACS Sustain. Chem. Eng. 28 (2020) 10335–10344.
[4] J.J. Richardson, J. Cui, M. Björnmalm, J.A. Braunger, H. Ejima, F. Caruso, Innovation in layer-by-layer assembly, Chem. Rev. 23 (2016) 14828–14867.
[5] D. Zhang, B.L. Williams, S.B. Shrestha, Z. Nasir, E.M. Becher, B.J. Lofink, V. H. Santos, H. Patel, X. Peng, L. Sun, Flame retardant and hydrophobic coatings on cotton fabrics via sol-gel and self-assembly techniques, J. Colloid Interface Sci. 505 (2017) 892–899.
[6] H. Wang, H. Liu, L. Kang, M. Chen, L. Tan, X. Yao, X. Chen, Z. Wu, S. Chen, J. Yu, D. Wu, molecularly engineered N/P/Si synergy on cotton fabric: dual-functional flame retardancy and antibacterial defense for hazard-safe textiles, Chem. Eng. J. 525 (2025) 170419.
[7] Y. Kong, X. Fan, R. Wu, S. Nie, C. Liu, X. Liu, G. Zhang, B. Yuan, Multifunctional flame-retardant cotton fabric with hydrophobicity and electrical conductivity for

wearable smart textile and self-powered fire-alarm system, Chem. Eng. J. 487 (2024) 150677.
[8] N. Selvakumar, A. Azhagurajan, T.S. Natarajan, M.M.A. Khadir, Flame-retardant fabric systems based on electrospun polyamide/boric acid nanocomposite fibers, J. Appl. Polym. Sci. 126 (2012) 614–619.
[9] J. Zhang, X. Mi, S. Chen, Z. Xu, D. Zhang, M. Miao, J. Wang, A bio-based hyperbranched flame retardant for epoxy resins, Chem. Eng. J. 381 (2020) 122719.
[10] I.S. Zope, S. Foo, D.G.J. Seah, A.T. Akunuri, A. Dasari, Development and evaluation of a water-based flame retardant spray coating for cotton fabrics, ACS Appl. Mater. Interfaces 9 (2017) 40782–40791.
[11] Y.C. Li, J. Schulz, S. Mannen, C. Delhom, B. Condon, S. Chang, M. Zammarano, J. C. Grunlan, Flame retardant behavior of polyelectrolyte−clay thin film assemblies on cotton fabric, ACS Nano 4 (2010) 3325–3337.
[12] Y.C. Li, S. Mannen, A.B. Morgan, S. Chang, Y.H. Yang, B. Condon, J.C. Grunlan, Intumescent all-polymer multilayer nanocoating capable of extinguishing flame on fabric, Adv. Mater. 23 (2011) 3926–3931.
[13] B. Boutevin, Y. Pietrasanta, The synthesis and applications of fluorinated silicones, notably in high-performance coatings, Prog. Org. Coat. 13 (1985) 297–331.
[14] A. Bentis, A. Boukhriss, M. Zahouily, B. Manoun, S. Gmouh, Functionalization of cotton fabrics by sol-gel method using ionic liquids with high-hydrophobic, excellent water repellent, oil/water separation, and self-cleaning properties, Cellulose 30 (2023) 6719–6740.
[15] J. Qian, Q. Dong, K. Chun, D. Zhu, X. Zhang, Y. Mao, et al., Highly stable, antiviral, antibacterial cotton textiles via molecular engineering, Nat. Nanotechnol. 18 (2023) 168–176.
[16] A. Ganguly, R.C. Brown, M.M. Wright, Techno-economic and greenhouse gas emission assessment of carbon negative pyrolysis technology, Green Chem. 24 (2022) 9290–9302.
[17] D. Laishram, S.B. Kim, S.Y. Lee, S.J. Park, Advancements in biochar as a sustainable adsorbent for water pollution mitigation, Adv. Sci. 12 (2025) 2410383.
[18] X. Li, M. Xie, J. Gao, K. Song, X. Li, J. Geng, J. He, R. Yang, Biomimetic sand-fixation-inspired flame retardants: enhanced char stabilization and multifunctional polyurethane with integrated fire safety, radiation shielding, and visual monitoring, Mater. Horiz. 12 (2025) 6899–6911.
[19] B. Yu, W. Xing, W. Guo, S. Qiu, X. Wang, S. Lo, Y. Hu, Thermal exfoliation of hexagonal boron nitride for effective enhancements on thermal stability, flame retardancy and smoke suppression of epoxy resin nanocomposites: via sol-gel process, J. Mater. Chem. A 4 (2016) 7330–7340.
[20] L. Lai, L. Chen, D. Zhan, L. Sun, J. Liu, S.H. Lim, C.K. Poh, Z. Shen, J. Lin, One-step synthesis of NH_2-graphene from in situ graphene-oxide reduction and its improved electrochemical properties, Carbon 49 (2011) 3250–3257.
[21] T. Sainsbury, A. Satti, P. May, Z. Wang, I. McGovern, Y.K. Gun'ko, J. Coleman, Oxygen radical functionalization of boron nitride nanosheets, J. Am. Chem. Soc. 134 (2012) 18758–18771.
[22] S. Pang, D. Peng, Y. Hao, B. Song, X. Zhang, L. Jiang, Regulating interlayer spacing of aminated graphene oxide membranes for efficient flow reactions, Matter 6 (2023) 1173–1187.
[23] A. Verma, H. Singh, Y. Mahton, P. Saha, C.S. Tiwary, J. Bhattacharya, Use of waste to wealth process derived sustainable silica-rich graphene analogues to provide enhanced corrosion resistance properties for coating on carbon steel, exposed to marine environments, Surf. Coat. Technol. 464 (2023) 129420.
[24] W. Zhu, X. Gao, Q. Li, H. Li, Y. Chao, M. Li, S.M. Mahurin, H. Li, H. Zhu, S. Dai, Controlled gas exfoliation of boron nitride into few-layered nanosheets, Angew. Chem. Int. Ed. 128 (2016) 10924–10928.
[25] R.S. Ambekar, A. Deshmukh, M.Y.S. Villagrán, R. Das, V. Pal, S. Dey, J.H. Miller, L. D. Machado, P. Kumbhakar, C.S. Tiwary, 2D hexagonal boron nitride-coated cotton fabric with self-extinguishing property, ACS Appl. Mater. Interfaces 12 (2020) 45274–45280.
[26] M. Pawlyta, J.N. Rouzaud, S. Duber, Raman microspectroscopy characterization of carbon blacks: spectral analysis and structural information, Carbon 84 (2015) 479–490.
[27] I. Ahmed, Z. Hasan, G. Lee, H.J. Lee, S.H. Jhung, Contribution of hydrogen bonding to liquid-phase adsorptive removal of hazardous organics with metal-organic framework-based materials, Chem. Eng. J. 430 (2022) 132596.
[28] H. Chen, Z. Yu, J. Ye, G. Yang, L. Chen, Y. Pang, et al., Chitosan functionalized hexagonal boron nitride nanomaterial to enhance the anticorrosive performance of epoxy resin, Colloids Surf. A Physicochem. Eng. Asp. 645 (2022) 128941.
[29] X. Zhang, S. Wang, W. Liu, C. Li, Progress in mechanical properties of carbon fiber composites: the role of graphene functionalization, Alex. Eng. J. 123 (2025) 519–529.
[30] Y. Liu, X. Wang, K. Qia, J.H. Xin, Functionalization of cotton with carbon nanotubes, J. Mater. Chem. 18 (2008) 3454–3460.
[31] K. Sarkar, D. Das, T.K. Chaki, S. Chattopadhyay, Macro-structured carbon clusters for developing waterproof, breathable conductive cotton fabric, Carbon 116 (2017) 1–14.
[32] J. Wang, K. Ai, L. Lu, Flame-retardant porous hexagonal boron nitride for safe and effective radioactive iodine capture, J. Mater. Chem. A 7 (2019) 16850–16858.
[33] P. Zhao, F. Xu, Y. Chen, T. Huang, G. Zhang, A novel durable flame retardant for cotton fabrics based on diethylenetriamine, Polym. Degrad. Stab. 195 (2022) 109796.
[34] Q. Ge, J. Chu, W. Cao, F. Yi, Z. Ran, Z. Jin, B. Mao, Z. Li, K.S. Novoselov, Graphene-based textiles for thermal management and flame retardancy, Adv. Funct. Mater. 32 (2022) 2205934.
[35] G. Han, X. Zhao, Y. Feng, J. Ma, K. Zhou, Y. Shi, C. Liu, X. Xie, Highly flame-retardant epoxy-based thermal conductive composites with functionalized boron nitride nanosheets exfoliated by one-step ball milling, Chem. Eng. J. 407 (2021) 127099.
[36] A. Shanu, K. Arun, V. Sajith, Flexible silicone rubber–silicon carbide heat spreader for heat removal from low-power electronics, Appl. Therm. Eng. 279 (2025) 127622.
[37] R. Karthik, A. Srivastava, S. Midya, A. Shanu, S. Slathia, S. Vandana, S. Kar, N. R. Glavin, A.K. Roy, P.R. Sreeram, A.K. Singh, C.S. Tiwary, Enhanced heat dissipation and reduced power consumption in electronics using 2D hexagonal boron nitride, Small 21 (2025) 2502007.
[38] T.S. Abhijith, S.S. Shijina, V.P. Muhammad Rabeeh, V. Sajith, Transient heat transfer studies of aluminium graphene nanocomposite heat spreaders using digital interferometry, Appl. Therm. Eng. 236 (2024) 121877.
[39] M. Li, S. Han, C. Dan, T. Wu, F. You, X. Jiang, Y. Wu, Z.M. Dang, Boron Nitride-Polymer composites with high thermal conductivity: preparation, functionalization strategy and innovative structural regulation, Small 21 (2025) 2412447.
[40] Z. Singh, R. Singh, Toxicity of graphene based nanomaterials towards different bacterial strains: a comprehensive review, Am. J. Life Sci. 5 (2017) 1–9.
[41] C. Nie, Y. Shi, S. Jiang, H. Wang, M. Liu, R. Huang, et al., Constructing fireproof MXene-based cotton fabric/thermoplastic polyurethane hierarchical composites via encapsulation strategy, ACS Appl. Polym. Mater. 5 (2023) 7229–7239.
[42] S. Bhattacharjee, C.R. Macintyre, X. Wen, P. Bahl, U. Kumar, A.A. Chughtai, R. Joshi, Nanoparticles incorporated graphene-based durable cotton fabrics, Carbon 166 (2020) 148–163.
[43] B. Abdi, A. Tarhini, H. Baniasadi, A.R.T. Bagha, Developing graphene-based conductive textiles using different coating methods, Adv. Mater. Technol. 9 (2024) 2301492.
[44] M.A. Jahid, J. Hu, K.H. Wong, Y. Wu, Y. Zhu, H.H.S. Luo, D. Zhongmin, Fabric coated with shape memory polyurethane and its properties, Polymers 10 (2018) 681.
[45] W. Guo, X. Wang, J. Huang, Y. Zhou, W. Cai, J. Wang, L. Song, Y. Hu, Construction of durable flame-retardant and robust superhydrophobic coatings on cotton fabrics for water-oil separation application, Chem. Eng. J. 398 (2020) 125661.
[46] C.H. Xue, Y. Wu, X.J. Guo, B.Y. Liu, H.D. Wang, S.T. Jia, Superhydrophobic, flame-retardant and conductive cotton fabrics via layer-by-layer assembly of carbon nanotubes for flexible sensing electronics, Cellulose 27 (2020) 3455–3468.
[47] E. Pakdel, J. Sharp, S. Kashi, W. Bai, M.P. Gashti, X. Wang, Antibacterial superhydrophobic cotton fabric with photothermal, self-cleaning, and ultraviolet protection functionalities, ACS Appl. Mater. Interfaces 15 (2023) 34031–34043.
[48] S. Chen, X. Li, Y. Li, J. Sun, Intumescent flame-retardant and self-healing superhydrophobic coatings on cotton fabric, ACS Nano 9 (2015) 4070–4076.
[49] H. Hassan, Z. Rehman, B.H. Koo, Eco-friendly fire-retardant coating on cotton using layer by layer deposition technique, Molecules 29 (2024) 5976.
[50] B. Xue, Y. Shi, C. Zhang, M. Niu, Y. Yang, Construction of a P–N–Si flame retardant coating on the cotton fabric with the integration of biomass carbon dots and ammonium polyphosphate, Cellulose 29 (2022) 9469–9486.
[51] H. Li, S. Xiao, H. Yu, Y. Xue, J. Yang, A review of graphene-based films for heat dissipation, New Carbon Mater. 36 (2021) 897–908.
[52] K. Nikolaos, P. Kyriaki, R. Claus, Thermal and chemical stability of hexagonal boron nitride (h-BN) nanoplatelets, Vacuum 112 (2015) 42–45.